Top Curr Chem (2010) 293: 77–113
DOI 10.1007/128_2009_4

Published online: 03 October 2009

Doping of Metal-Organic Frameworks with Functional Guest Molecules and Nanoparticles

Felicitas Schröder and Roland A. Fischer

Abstract Nanoparticle synthesis within metal-organic frameworks (MOFs) is performed by the adsorption of suitable precursor molecules for the metal component and subsequent decomposition to the composite materials nanoparticles@MOF. This chapter will review different approaches of loading MOFs with more complex organic molecules and metal-organic precursor molecules. The related reactions inside MOFs are discussed with a focus on stabilizing reactive intermediates in the corresponding cavities. The syntheses of metal and metal oxide nanoparticles inside MOFs are reviewed, and different synthetic routes compared. Emphasis is placed on the micro structural characterization of the materials nanoparticles@MOF with a particular focus on the location of embedded nanoparticles using TEM methods. Some first examples of applications of the doped MOFs in heterogeneous catalysis and hydrogen storage are described.

Keywords Catalysis • Hydrogen storage • Metal oxides • Metal-organic frameworks • Nanoparticles

Contents

F. Schröder and R.A. Fischer (✉)
Lehrstuhl für Anorganische Chemie II-Organometallics and Materials,
Ruhr Universität Bochum, Germany
e-mail: roland.fischer@rub.de

Abbreviations

bdc	1,4-Benzene-dicarboxylate
bpdc	4,4′,-Biphenyldicarboxylate
BPTC	1,1´-Biphenyl-2,2´,6,6´-tetracarboxylate
CN^{t}Bu	Tertiary-butyl isonitrile
cod	*cis*,*cis*-1,5-Cyclooctane
COF	Covalent organic framework
cot	*cis*,*cis*,*cis*-1,3,5-Cyclooctatriene
Cp	Cyclopentadienyl-anion (C_5H_5)
cyclam	1,4,8,11-Tetraaza-cyclotetradecane
dabco	1,4-Diazabicyclo[2.2.2]octane
DMA	*N*,*N*-Dimethylacetamide
dmf	Dimethylformamide
EXAFS	Extended X-ray absorption fine structure
FT-IR	Fourier transform infrared spectroscopy
FWHM	Full width at half maximum
HAADF	High-angle annular dark field
HKUST	Hong Kong University of Science and Technology
JUC	Jilin University China
Me	Methyl
MIL	Matérial Institute Lavoisier
MOCVD	Metal-organic vapor deposition
MOF	Metal-organic framework
mtb	methanetetra-benzoate
O*i*Pr	Iso-propoxide
pyz	Pyrazine
SAED	Selected area electron diffraction
STEM	Scanning transmission electron microscopy
TATB	triazine-1,3,5-tribenzoate
TEM	Transmission electron microscopy
THF	Tetrahydrofuran
wt%	Weight percent
XANES	X-ray absorption near edge structure
XAS	X-ray absorption spectroscopy
XRD	X-ray powder diffraction
ZIF	Zeolite A imidazolate framework

1 Introduction

Metal-organic frameworks (MOFs) allow reversible adsorption of guest molecules and are thus characterized by a permanent porosity. This novel class of hybrid inorganic–organic soft solid state materials is largely based on Werner-type coordination chemistry. Specifically, the research on porous coordination polymers has become a major field of research during the past decade [1–8]. For example, the concepts of "reticular synthesis," along with the basic zinc and copper carboxylates based so-called MOFs [9,10] were established; likewise boronic ester based frameworks (COFs) [7] and zinc imidazolate based MOFs (ZIFs) [13–15] were also introduced. The responsive and adaptive properties of soft porous coordination polymers with applications in gas storage, sensing and catalysis have been investigated as well [16–19]. The so-called Materials of Institute Lavoisier (MILs) [20,21], were introduced, with MIL-53 and MIL-88 demonstrating large and reversible structural changes upon guest exchange and MIL-101 being the most porous material known to date, with an equivalent Langmuir surface area of 5,900 $m^2 g^{-1}$ [22]. Chiral MOFs, e.g., with an amino acid backbone, exhibiting interesting properties in selective solvent sorption have been studied [23]. A wide range of studies on the applications of all these materials in gas storage and separation as well as solvent separation have been performed [15,25–33]. Furthermore the controlled growth of MOF thin films at surfaces ("SURMOFs") has been demonstrated by a few groups recently [34–38]. This paves the way for integration of MOF materials into more complex functional devices such as smart membranes and chemical sensors. Herein we will focus on the doping of MOFs with nanoparticles. Similar to zeolites, mesoporous silica and other inorganic porous materials, the grafting of functional molecular species at the internal surface of MOFs and the loading of the pores, cavities or channels of MOFs with functional nanoparticles is relevant for a number of potential applications including catalysis, hydrogen storage and sensing [39–44]. In addition, the use of MOFs as host materials for the formation of nanosized metals or metal oxides is of considerable interest as it helps to study the resulting specific properties and host-synergetic functions [45–47]. In this chapter we will cover the current literature related to the doping of MOFs with nanoparticles with some emphasis on the involved precursor concepts. The discussion will include relevant aspects of the loading of MOFs and loading-related properties in general. This appears to be very important since the loading of MOFs, using molecular precursors to provide the components for the nanoparticle growth inside the framework, clearly relies on the supramolecular host–guest chemistry of MOFs in general.

2 Loading of Metal-Organic Frameworks with Guest Molecules

The synthesis of MOFs usually requires the pores or channels to be occupied with solvent molecules and sometimes also with unreacted, excess linkers. These molecules should be removable or exchangeable by other solvent or gas molecules

without any structural change of the parent framework in order to load MOFs with more complex functional molecules. This is apparently mandatory, since in some cases structural changes of the host or even complete collapse of the framework structure can occur upon solvent removal [17,18]. MOFs are typically studied in the context of their gas storage and/or separation properties, mainly focusing on rather nonpolar hydrocarbons [25–33]. Most MOFs exhibit nonpolar, i.e., hydrophobic, inner surfaces and we will largely restrict our discussion to these types of MOFs.

2.1 Large Organic Molecules

Only a few key examples of MOFs have been tested in loading with larger, more complex organic molecules so far. In their first report on the zinc-1,3,5-benzenetribenzoate based MOF-177 in 2004 [10], Yaghi et al. introduced loading of this highly porous framework with dye molecules of Astrazon Orange R, Nile red and Reichardt's dye as well as with C_{60} molecules. The inclusion of these compounds in MOF-177 was followed by UV- and Raman-Spectroscopy (Fig. 1). Quantitative uptake analysis of the materials revealed sixteen molecules of Astrazon Orange R, two molecules of Nile red and one molecule of Reichardt's dye per MOF-177 unit cell, already demonstrating the size dependant sorption properties of MOF-177.

Quiu et al. presented the synthesis of the porous framework $[Cd_3(bpdc)_3(dmf)]\cdot 5\,dmf\bullet 18\,H_2O$ (bpdc = 4,4′-biphenyldicarboxylate, dmf = dimethylformamide, JUC-48, JUC = Jilin University China) and the assembly of Rh6G dye molecules in its pores [48]. The dye molecules were infiltrated by either adding an ethanolic solution of the dye to the mother liquor of the MOF or immersion of the framework in the dye solution. The dye@MOF composite showed temperature dependent fluorescence properties. Férey et al. studied the loading of the chromium terephthalate based MIL-101 with the Keggin anion $[PW_{11}O_{40}]^{7-}$ in order to show the selective inclusion of very large guest molecules into the spacious cages of the MIL-101 (Fig. 2) [22]. The loading was followed by powder X-ray diffraction (PXRD), N_2 adsorption and ^{31}P-NMR. From elemental analysis 0.05 Keggin anions per chromium were found, corresponding to a loading of five Keggin moieties per large cage of MIL-101. The volume of five Keggin anions represents 10,100 Å^3 in volume, the volume of the large cage of MIL-101 however is 20,600 Å^3, and the authors therefore assume that the remaining space is filled with cations and water molecules. The Férey group also introduced the first drug (Ibuprofen) release study of a MOF [49,50]. The Ibuprofen uptake of the frameworks as well as the subsequent release were investigated.

Leaving the well known toxicity of chromium aside, the drug release study of MIL-101 and MIL-100 shows the potential of MOFs for not only the loading but also the controlled release of an imbedded compound [49]. MIL-101 is able to take up four times as much Ibuprofen as MCM-41, which has comparable cage sizes. It also shows a slower delivery rate, which presents advantages for larger

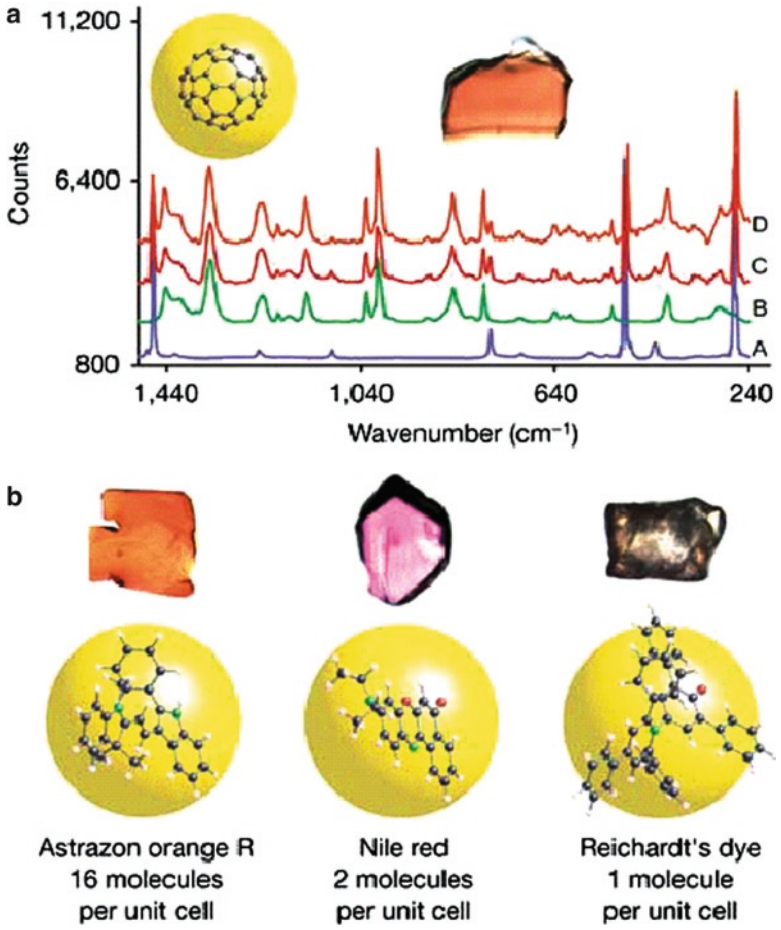

Fig. 1 Loading of MOF-177: (**a**) Raman spectra of (A) bulk C_{60}, (B) evacuated MOF-177 crystal, (C) whole MOF-177 crystals loaded with C_{60} and (D) sliced MOF-177 crystals loaded with C_{60}. (**b**) MOF-177 crystal loaded with dye molecules.[10] Reprinted by permission from Macmillian Publishers Ltd: [Nature] [10] copyright 2004

pharmacological molecules. Very recently, the "breathing" chromium and iron based MIL-53 materials have also been used as matrices for the delivery of Ibuprofen [50]. Very slow, controlled and complete delivery was achieved under physiological conditions which are due to the ability of the framework to adapt to the dimensions of the drug.

These and similar studies employing more complex organic molecules as guests prove distinct features of the corresponding framework, like extraordinary cavity size or adsorption properties. The loading of MOFs with metal-organic precursor molecules is effected by the combination of the functionality of the precursors to

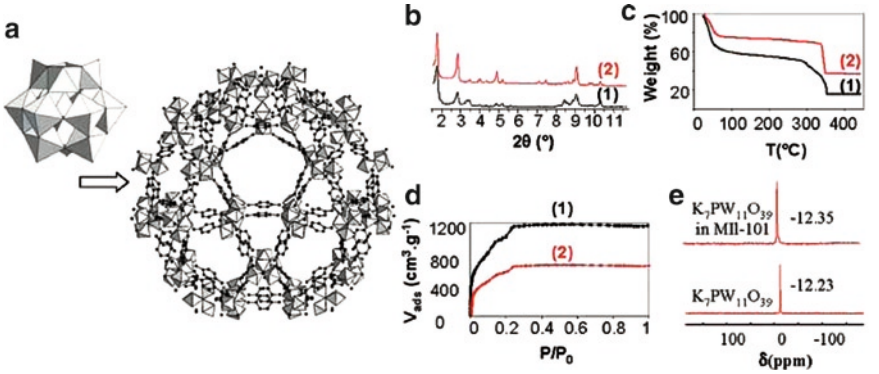

Fig. 2 (**a**) Schematic view of the insertion of Keggin anions within the largest pore of MIL-101. (**b**) XRD of MIL-101 (1) and MIL-101(Keggin) (2). θ, in degrees. (**c**) TGA of MIL-101 (1) and MIL-101(Keggin) (2). *T*, temperature (K). (**d**) Nitrogen sorption–desorption isotherms at 78 K of MIL-101 (1) and MIL-101(Keggin) (2). V_{ads}, volume adsorbed in cm^3g^{-1}. (**e**)^{31}P solid state NMR spectra of the Keggin salt and MIL-101(Keggin). δ, chemical shift in ppm. From [22]. Reprinted with permission from AAAS

serve as sources for nanoparticles, with the property of the MOF to restrict the growth and the aggregation of the particles by caging effects. Interestingly, the characteristic sizes of cavities, channels and pores of MOFs cover a size regime between classical zeolites ≤1 nm and mesoporous materials ≥2–3 nm. In contrast to these latter materials however, MOFs are expected to show a much weaker particle/host interaction.

3 Towards Nanoparticles in Metal-Organic Frameworks

Metal doping of MOFs seems to be a promising field of research not only for catalytic applications but also for enhanced capacity in gas storage as compared to the pure MOF [51]. In general one could think of two different approaches for the synthesis of metal nanoparticles inside MOFs: the infiltration of preformed nanoparticles stabilized by organic molecules (surfactants) in solution or the stepwise infiltration of suitable precursors and their conversion into nanoparticles inside the framework cavity. For other porous host materials, such as silica and alumina, several approaches for embedding nanoparticles in their cavities via immersion in colloidal solutions are known in the literature [52,53]. However, the typical cavity sizes of MOFs are too small to match the size of surfactant stabilized nanoparticles with hydrodynamic radii typically larger than 3 nm. In order to utilize the MOF as a stabilizing agent and host material at the same time, stepwise precursor infiltration and subsequent decomposition appear to constitute the most suitable approach. In this way, the size and shape of the nanoparticles, synthesized directly in the pores

of the framework, should be controlled by the pore size, shape and channel structure of the host material. Suitable precursors for the synthesis of metal nanoparticles in MOFs can in general be molecules that are also commonly used in the synthesis of colloidal metal nanoparticles in solution or metal nanoparticles in the solid state. These molecules are often also known from thin film formation processes such as metal-organic vapor deposition (MOCVD) or atomic layer deposition (ALD) and are basically metal-organic coordination compounds, the so-called organometallic compounds, often with entirely hydrocarbon ligand molecules, featuring metal carbon bonds. Upon decomposition, the ligands of these molecules are cleaved from the metal center, leaving "free" metal atoms that will then fuse together to form metal clusters [54,55]. Spatial confinement of the MOF cavities should limit the growth of the particles to the size of the corresponding pore diameter. Note, that the host framework should be inert towards the embedded precursor as well as to decomposition products or free ligands of the precursor molecules. Here, common approaches known from colloid and nanoparticle chemistry in general, like the "polyol process" for coinage and noble metal colloids seem to have a somewhat lower importance due to the reactivity of many MOFs toward acidic conditions (protons) and halides, especially at elevated temperatures. That typical metal-organic precursor molecules often exhibit an intrinsic reactivity toward protic solvent residues, hydroxyl groups or other reactive groups inside the host material, should not also be overlooked. Thus, a careful choice of the MOF and the precursor is mandatory for a controlled nanoparticle synthesis inside a MOF. We will now discuss the loading of MOFs with metal-organic coordination complexes and related precursors for metal nanoparticles.

3.1 Loading with MOCVD Precursors

Loading of metal-organic frameworks with MOCVD precursor molecules can be seen as an extension of the loading with larger nontrivial organic molecules as mentioned above. Some of these coordination compounds are highly volatile already at room temperature; others are sublimable at elevated temperature and pressure. Loading of MOFs with these compounds can therefore be compared to loading with gases or volatile solvents and is usually performed in vacuum. With respect to the subsequent controlled decomposition of the included molecules to nanoparticles, MOCVD precursors are a suitable class of compounds for the loading of MOFs. For a controlled loading, the characterization of the primary inclusion compounds precursor@MOF is required to afford a well-defined metal@MOF composite in a second step. In addition, studying the loading process of the MOF with precursor molecules also offers interesting insights into the host–guest interactions of this composite which may help to elucidate the interactions between imbedded metal nanoparticles and the MOF. This is highly relevant since catalytic processes, for example, often demand well-defined host–guest interactions to enable stabilization of free adsorption sites for molecules in the catalytic reaction.

Depending on the guest molecules, loading of MOFs can be generally performed via the gas phase under vacuum or via solution. In all studies discussed above, loading of MOFs with dye molecules [10,48], C_{60} [10], Keggin anions [22] and Ibuprofen [49,50] was performed via solution impregnation of the MOF powders. The MOF materials were immersed in saturated solutions of the compounds, allowing the guest molecules to diffuse slowly into the MOF cavities. When loading via solution, the competition in diffusion between the guest and the solvent molecules has to be taken into account. A uniform distribution of the guest molecules throughout the framework is not easy to achieve due to the inclusion of solvent molecules at the same time [10]. Kaskel et al. have used the "incipient wetness technique" to load MOF-5 with the Pd precursor [$Pd(acac)_2$] (acac = acetylacetonate) [51]. The advantage of this technique is the rather precise control of the loading just by choosing a certain concentration of the precursor in the solution. With this technique however, the loading with precursors is limited to the solubility of the precursor molecule in the solvent used. Note that, Kaskel et al. introduced only 1 wt% Pd into MOF-5, which is however, fine for many catalytic applications. Due to its facile synthesis even in larger scales, temperature stability up to 400°C in argon, high Langmuir surface area of up to 4,400 $m^2 g^{-1}$ [56] and the relatively large pore opening of 7.8 Å [6], MOF-5 is quite a nice test system for various types of loading studies. However, the reactivity of MOF-5 towards water and humid air [57,58] limits its application in technical processes to some extent. The first studies on the loading of MOFs with MOCVD precursor molecules and the subsequent synthesis of metal nanoparticles in MOF (which we will discuss later), have been performed by infiltration of [$CpPd(\eta^3\text{-}C_3H_5)$], [$CpCu(PMe_3)$] and [$Au(CH_3)(PMe_3)$] in MOF-5 ($Zn_4O(bdc)_3$, bdc = benzene-1,4-dicarboxylate) in vacuum [59].

Thus, freshly prepared [$Zn_4O(bdc)_3$] was activated in vacuum and then exposed to the vapors of the different metal-organic molecules. The loading was followed by ^1H and ^{13}C MAS-NMR, FT-IR, PXRD and elemental analysis. It was shown that similar to the loading with the large organic molecules, the structure of the host framework remains intact after inclusion of the MOCVD precursor compounds. The presence of the unchanged guest molecules inside the MOF cavities was shown by the corresponding solid state ^1H and ^{13}C MAS-NMR signals and elemental analyzes. In a second, more detailed study, the loading of MOF-5 was extended to a variety of metal and metal oxide precursors, here different aspects of the loading were investigated [61]. The metal loading was in a range of 10–40 wt% (see Table 1). The reversible loading of MOF-5 was presented, without changing the chemical properties of the precursors or the host framework.

Ferrocene, as a representative example for many organometallic compounds of interest here, can be first infiltrated into the MOF-5 cavities (see Fig. 3) and can then be removed without any change of the host material. Also, the dependence of the size of the precursor molecules on the loading was shown. MOF-5 cavities exhibit an opening diameter of 7.8 Å. Ideally, only one of the three principal axes (x, y, z; see Table 2) of the enveloping ellipsoid representing the van der Waals volume of the respective precursor molecule should exceed this diameter in order to allow diffusion into the MOF cavities. For that reason, [$Cu(OCHMeCH_2NMe_2)_2$]

Table 1 Loading parameters of various precursors in MOF-5 and MOF-177

MOF-5				
	Elemental analysis (measured/calculated)			
Precursor	M (%)	C (%)	H (%)	Calculated number of molecules
$[CpPd(\eta^3\text{-}C_3H_5)]$	26.4/26.3	41.5/41.5	3.14/3.2	4
$[CpPtMe_3]$	34.5/34.7	34.2/34.2	3.0/3.2	3
$[FeCp_2]$[a]	–	54.22/54.49	3.98/3.99	7
$[CpCu(CN^tBu)]$	6.4/6.5	41.2/41.6	2.6/2.6	1
$[CpCu(PMe_3)]$	10.7/10.8	40.4/40.7	3.4/3.4	3
$[Au(CH_3)\ (PMe_3)]$	40.8/41.0	23.4/24.9	3.4/3.1	3
$[Sn(C_4H_9)_2(OOC_2H_3)_2]$	8.7/–	38.5/–	2.8/–	0.75
$[Zn(C_2H_5)_2]$	41.8/42.0	31.1/30.9	1.3/1.29	2
$[CpPd(\eta^3\text{-}C_3H_5)]/[CpPtMe_3]$	12.2/–; 16.7	38.1/–	3.75/–	1.70;1.76
MOF-177				
$[CpPd(\eta^3\text{-}C_3H_5)]$	31.9/32.4	47.7/48.9	3.8/4.3	11
$[CpCu(PMe_3)]$	8.3/8.2	49.6/53.9	3.8/3.8	10
$[CpCu(CN^tBu)]$	8.3/8.2	50.9/56.5	3.8/3.7	2
$[FeCp_2]$	19.4/19.1	60.3/61.2	4.5/4.4	2
$[ZnCp^*_2]$	19.1/21.4	63.5/62.2	8.1/3.3	2

[a]Loading parameters for $[FeCp_2]$@MOF-5 were taken from Kim et al. [60]

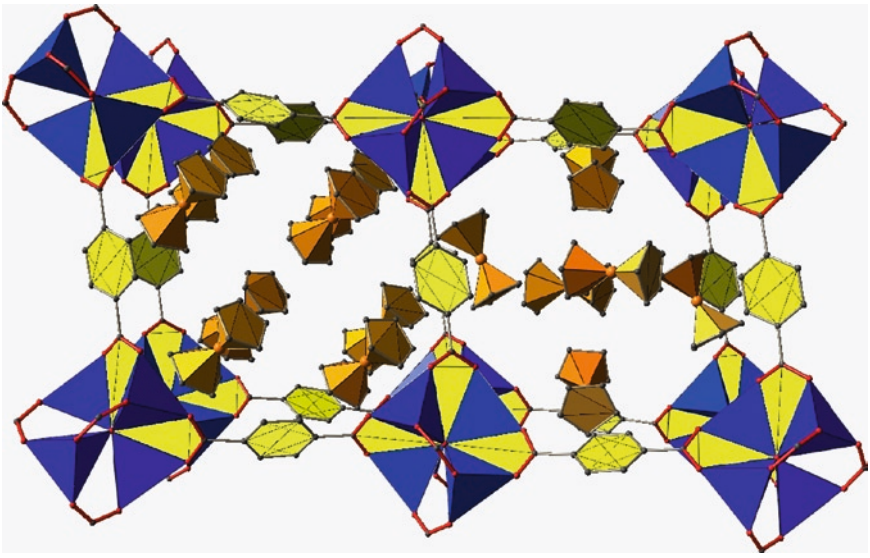

Fig. 3 Cut-out of the crystal structure [60] of the inclusion compound ferrocene$_7$@MOF-5

Table 2 Characteristic molecular dimensions of organometallic precursors absorbed by MOF-5 and MOF-177

Precursor	*x*	*y*	*z*	Max.
[CpPd(η^3-C_3H_5)]	4.5	4.5	4.5	5.5
[CpPtMe_3]	4.3	4.7	4.7	6.5
[$FeCp_2$][a]	3.5	4.5	4.5	5.2
[CpCu(CN^{t}Bu)]	4.5	4.5	7.6	8.2
[CpCu(PMe_3)]	5.0	5.0	7.5	7.5
[Au(CH_3)(PMe_3)]	4.5	4.5	7.0	7.0
[Sn(C_4H_9)$_2$(OOC_2H_3)$_2$]	6.5	7.8	10.0	10.0
[Zn(C_2H_5)$_2$]	1.8	3.0	8.0	8.0
[$Fe(CO)_5$]	4.2	4.2	5.9	5.9
[Cu($OCHMeCH_2NMe_2$)$_2$]	6.5	7.9	8.7	8.7

[a]*x*, *y*, *z* in Å

is not adsorbed by the MOF-5 matrix since its characteristic dimensions exceed the pore opening in all three dimensions (see Table 2). Not surprisingly, the loading is also dependent on the vapor pressure of the precursor molecule. Rapid desorption is observed for small, comparably volatile compounds such as [$Fe(CO)_5$] or [Zn(C_2H_5)$_2$]. Cyclopentadienyl complexes such as [$FeCp_2$] form more stable inclusion compounds with the MOF-5 matrix. More or less stoichiometric inclusion compounds of the formula precursor$_n$@MOF-5 (where n is the average number of precursor molecules per MOF-5 cavity) are obtained in all cases according to elemental analytical data (see Table 1). In addition to this, the loading of MOF-177, another member of the zinc(II) carboxylate based MOFs, with MOCVD precursor molecules has been studied [62,63]. The larger pore opening and pore volume of MOF-177 (10.8 Å and 1.59 $m^2 g^{-1}$ [10]) in comparison to MOF-5 (7.8 Å and 1.04 $m^2 g^{-1}$ [6]), allows the diffusion of larger molecules like [Cu($OCHMeCH_2NMe_2$)$_2$] into the cavities, and the overall absorption of more molecules per cavity than in MOF-5 [63]. Typically the included precursor molecules are very mobile and behave as in solution. This was concluded from the comparison of the solid state NMR of the samples precursor@MOF with the respective high resolution NMR data of the precursors in solution [61]. When the precursors are intercalated in MOF-5, they exhibit the same number of signals with almost the same chemical shift as in solution. This indicates a low interaction with the host framework and the high mobility of the precursor molecules. For example, the solid state ^{13}C MAS-NMR of [Ru(cod)(cot)]@MOF-5 (cod = 1,5-cyclooctadienyl, cot = 1,3,5-cyclooctatrienyl) exhibits six signals for the carbon centers of the intercalated precursor, corresponding to the number of signals of [Ru(cod)(cot)] in C_6D_6 solution [64]. In contrast, the solid state ^{13}C MAS-NMR of the pure, crystalline Ru precursor exhibits 16 signals, i.e., each carbon center of the ligands is different. MAS-NMR and FT-IR spectroscopy and PXRD are very powerful techniques to follow guest inclusion in porous materials. The loading of MOF-5 with [Ru(cod)(cot)] was also followed by means of the change of MOF-5 PXRD reflection intensities below 10° 2θ.

In general, the overall intensity of the host XRD reflections will decrease upon inclusion of guest molecules due to the enhancement of the X-ray scattering contrast [65]. In MOF-5, the intensity ratio of the reflections at especially $2\theta = 6.9°$ and 9.7° will change upon loading [66]. This is also observed when the powder X-ray data of pure, empty MOF-5 and [Ru(cod)(cot)]@MOF-5 are compared (see Fig. 4); the intensities of these peaks are inverted. Most noteworthy, the PXRD of [Ru(cod)(cot)]@MOF-5 displays many additional reflections which originate from the ordering of the guest molecules in the MOF-5 with new reflections observed at $2\theta = 10–20°$, with the most prominent new reflection at 13.8°. However, the exact structure of the material [Ru(cod)(cot)]@MOF-5 could not be fully elucidated with Rietveld analysis. Usually the embedded precursor molecules are randomly distributed which is deduced from the almost unchanged PXRD of the host matrix, i.e., lacking new extra diffraction peaks and only showing some more or less pronounced intensity deviations. However, investigating the ordering of organometallic molecules in the MOF cavities is clearly an interesting aspect of loading of MOFs in general. Only in a few cases can a crystal structure of the host–guest composite be obtained. The first example of such a substructure was investigated by Kim et al. [60]. Similar to the first reports by us, MOF-5 was loaded with ferrocene via gas phase in vacuum. Interestingly, the authors attempted loading of MOF-5 in dimethylformamide (DMF) solution as well. However in this case, inclusion of the guest molecules was not successful as shown by UV/VIS spectroscopy (see our above comments regarding solution impregnation). By applying synchrotron radiation at 100 K, a single crystal structure of the compound $[FeCp_2]_7$@MOF-5 was obtained. Shrinkage of the unit cell volume of 3.7% is observed compared to the evacuated host.

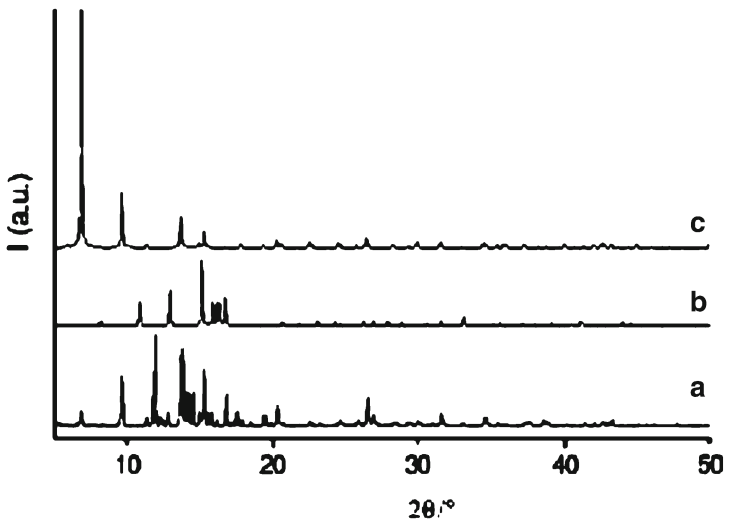

Fig. 4 Powder X-ray diffractogramms of (**a**) [Ru(cod)(cot)]@MOF-5, (**b**) [Ru(cod)(cot)] and (**c**) MOF-5. Reproduced with permission from [64]. Copyright 2008 American Chemical Society

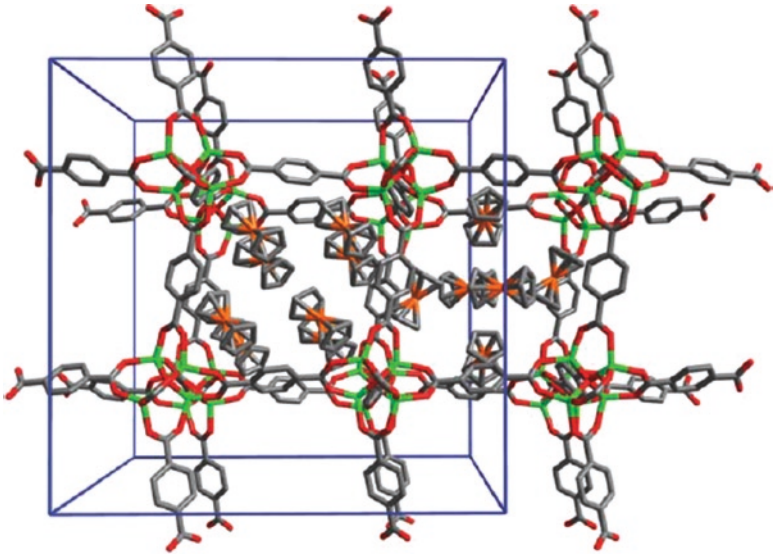

Fig. 5 Single crystal structure of $[FeCp_2]_7$@MOF-5 [60]. Reproduced by permission of the Royal Society of Chemistry

The unit cell is defined by the space group *Pa-3*. The smaller pores of MOF-5 are filled with six ferrocene molecules; the larger pores with eight (see Fig. 5) [60]. Depending on the tilting of the *bdc* linkers, MOF-5 exhibits two kinds of pore diameters with 11.0 and 15.1 Å [6]. From elemental analysis the results of the crystal structure were confirmed, giving seven ferrocene molecules per formula unit of MOF-5, which corresponds to 56 ferrocene molecules per elementary cell of the MOF-5 structure. The six ferrocene molecules in the smaller pore adopt an octahedral arrangement with the ferrocene molecules close to the faces of the cube shaped cavity. The eight molecules in the larger pore are positioned near the corners of the MOF-5 pores (see Fig. 6). Here extensive π–π interactions exist between the guest molecules as well as between the guests and the framework itself. The packing of the ferrocene molecules in the pores leaves only 1.6% of the crystal volume accessible to other guest molecules.

In another study, Kim et al. have shown the loading of porous $[Tb_{16}(TATB)_{16}(DMA)_{24}](DMA)_{91}(H_2O)_{108}$ (TATB = triazine-1,3,5-tribenzoate, DMA = *N,N*-dimethylacetamide) with ferrocene [67]. In this case, a crystal structure of the composite was not obtained. Loading was followed by emission spectroscopy and ^{1}H-NMR spectroscopy with elemental analytical data suggesting 65 ferrocene molecules per formula unit. It is important to mention that it is not at all straightforward to obtain the superstructure of the guest molecules inside MOFs. As discussed above, at least in MOF-5, which exhibits no additional functional groups at the *bdc* linkers, the interaction between intercalated guests and the host is comparatively low with the intercalated guest molecule behaving almost as in a solid solvent cage. Therefore, X-ray diffraction

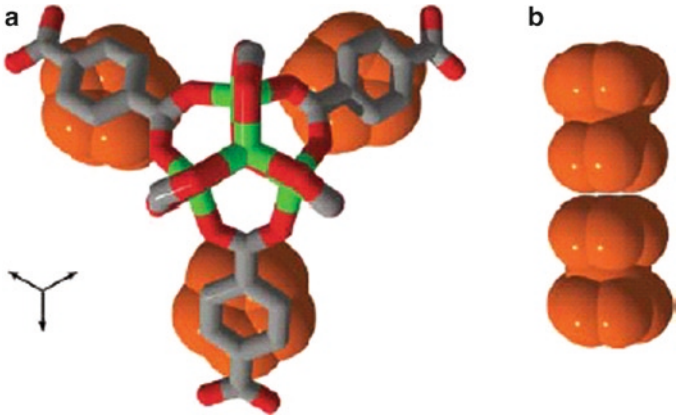

Fig. 6 The orientation of the ferrocene molecules in the larger pore of MOF-5 [60]. Reproduced by permission of the Royal Society of Chemistry

measurements should be performed at low temperatures, thus reducing mobility in order to obtain a high quality data set. In addition, the reflections of the guest structure are often rather weak, which demands the use of high intensity X-rays, e. g. synchrotron radiation for collecting diffraction data. However, the crystal structure of ferrocene@MOF-5 nicely shows the influence of the space limitation of the MOF cavities on the ferrocene arrangement and conversely, the subtle effects of the loading on the MOF-5 framework itself. This leads to another aspect of loading MOFs. The space confinement of the MOF cavities may also support and stabilize reactive species as intermediates of organometallic or organic reactions.

3.2 Reactions Inside MOFs

The interior of porous hosts may be very different from that of the exterior surroundings, leading to a novel kind of reactive species in these pores. For example, reactive intermediates from metal-organic or organic reactions could possibly be stabilized in the cavities of the host material.

At this point, it is noteworthy, that detailed studies on the stabilization of reactive species inside metal-organic polyhedrons have already been performed. Here, the group of Raymond et al. has given interesting insights into the rich host–guest chemistry of the assemblies of the type M_4L_6 (see Fig. 7) [68,69]. For instance, it was shown that the ionic $[(Cp)Ru(cod)]^+$ and $[(Cp^*)Ru(\textit{cis}\text{-}1,3,7\text{-octatriene})]^+$ species, which usually rapidly decompose in water, are stabilized inside the cluster $[Ga_4L_6]^{12-}$ in aqueous solution [70]. Despite their stabilization within the host, the guest molecules are still able to react stoichiometrically with CO. In addition, the ability of the tetrahedral assemblies to act as nanoenzymes, catalyzing the hydrolysis of acetals and ketals in basic solution has been presented [71]. In a similar metal-organic

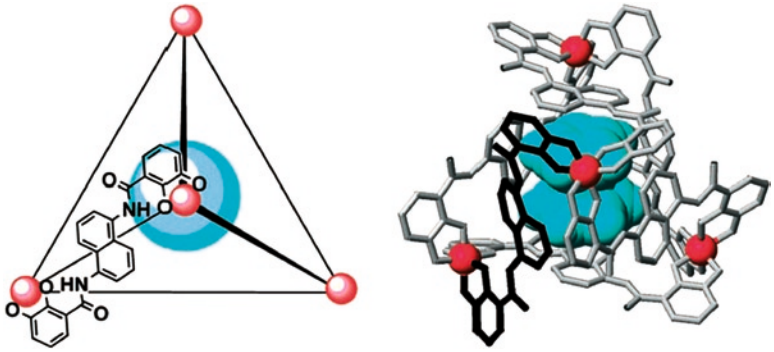

Fig. 7 Schematic presentation of the supramolecular tetrahedral assembly Ga_4L_6 a guest molecule included in the nanocage [57,58]. Copyright Wiley-VCH Verlag GmbH & Co. KGaA. Reproduced with permission

polyhedron even the observation of a reactive intermediate of the photodissociation of [Cp´Mn(CO)$_3$] by crystal structure was shown by Fujita et al. [72] with the in situ generated pyramidal [Cp´Mn(CO)$_2$] observed directly by X-ray diffraction.

These results suggest that MOFs as "extended" metal-organic assemblies could show a similar host–guest chemistry. In uncharged MOFs however, space confinement should be the most effective stabilizing effect on these species.

So far only few reports on reactions inside MOF and the trapping of reactive intermediates have been published. The first example was reported by Long et al. who showed functionalization of MOF-5 *bdc* linkers with {Cr(CO)$_3$} fragments and subsequent photoreactions [73]. The fragments were introduced by heating the MOF-5 powder in a solution of Cr(CO)$_6$ in THF/Bu$_2$O. Photoreactions of the {Cr(CO)$_3$} fragment with N_2 and H_2 lead to stable (η^6-arene)Cr(CO)$_2$(N_2) and (η^6-arene)Cr(CO)$_2$(H_2) species which are usually only accessible in frozen gas matrices or supercritical fluids (Fig. 8). Thus, the MOF framework shows a remarkably stabilizing effect on the reactive fragments. Another example of reactions inside a MOF was presented by us. The hydrogenolysis of [Ru(cod)(cot)] inside MOF-5 at atmospheric H_2 pressure led to the formation of (η^6-arene)Ru(cod) species with the *bdc* linkers of MOF-5 as a side- product of Ru nanoparticle formation in the framework [64]. This is in full agreement with known arene/cot exchange reactions of [Ru(cod)(cot)] taking place when the precursor is treated with 1 bar H_2 in the presence of arenes in solution. In contrast to the work of Long et al., not all *bdc* linkers were coordinated by {Ru(cod)}, and ^{13}C MAS-NMR showed signals of "free" *bdc* linkers. Here, obviously diffusion limitation inside the framework causes incomplete splitting of the alkene ligands of the Ru precursor by hydrogenolysis, and this enables coordination of {Ru(cod)} fragments to a fraction of the aromatic moiety of the *bdc* linkers. So far, there are no reports in the literature on molecular complexes of the {Ru(cod)} fragment and terephthalic acid or its derivatives. Evidently, the caging effect of MOF-5 has an influence on the kinetics of the hydrogenolysis of [Ru(cod)(cot)] leading to partial functionalization of *bdc* linkers with {Ru(cod)} fragments.

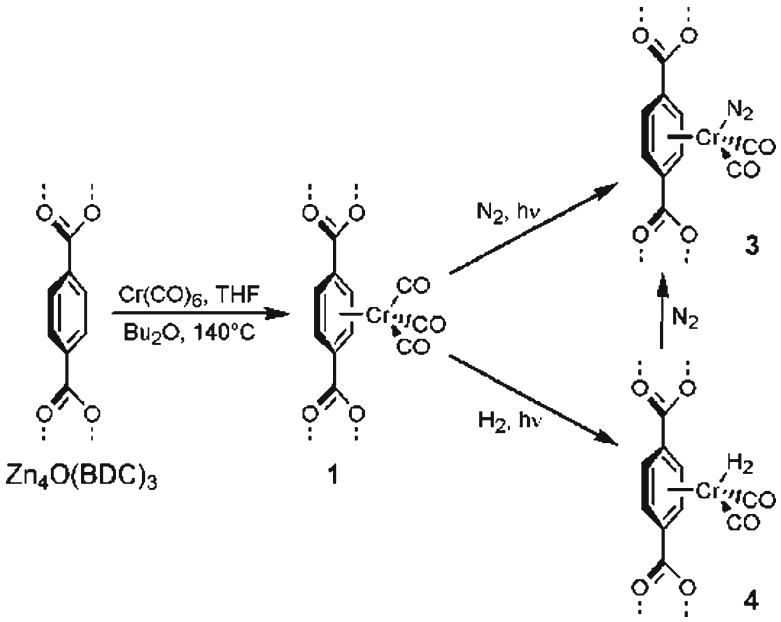

Fig. 8 Reaction of $[Zn_4O(bdc)_3]$ with $Cr(CO)_6$. Reproduced with permission from [73]. Copyright 2008 American Chemical Society

From these first examples it can be concluded that MOFs, especially MOF-5, show potential as stabilizing matrices for reactive intermediates in metal-organic reactions. In the future this will definitely be studied in more detail.

4 Nanoparticles Inside Metal-Organic Frameworks

The synthesis of nanoparticles inside MOFs is another, still more special example of reactions inside the framework. Nanoparticles "trapped" inside MOF cavities, with a high number of reactive surface atoms, are indeed reactive species as well. Their synthesis inside the porous hosts, starting from molecular precursors, anticipates the caging effect of the framework. To prevent the clusters from growing to larger, bulk agglomerates, the space confinement of the framework pores is utilized naturally.

4.1 General Synthesis

In the few reports of the synthesis of nanoparticles inside MOFs, the formation of nanoparticles is obtained in two steps: loading of the porous host with precursor molecules followed by decomposition of the precursors inside the porous host.

Depending on the properties of the intercalated precursor, the decomposition conditions have to be chosen carefully. In general, decomposition of MOCVD precursors can be achieved by treatment with reactive gases such as H_2 at a suitable temperature, by treatment at an elevated temperature or by photolysis. The formation of nanoparticles from metal salts, i.e., loading the MOFs with metal cations or inorganic metal complexes, e.g., $[PdCl_4]^{2-}$ as precursors, will be addressed as a special case later. It is mandatory to choose precursors with decomposition conditions that will be tolerated by the host framework. Therefore, the thermal stability of the framework should match the corresponding decomposition temperature of the precursor in order to obtain nanoparticles in an unchanged host matrix. Also, the stability of the MOF towards possible additional reactive gases or UV radiation has to be confirmed. For different precursors, different decomposition protocols have to be applied. The obtained nanoparticle@MOF composites can subsequently be investigated by analytical techniques such as PXRD, X-ray absorption spectroscopy (XAS), N_2 sorption measurements and transmission electron microscopy (TEM). As for related research on nanoparticles hosted by zeolites or mesoporous silica, the challenge is to determine whether the nanoparticles are located inside or outside the framework and to investigate and control the distribution of the particles inside the matrix. Beside TEM, routine analytical methods only give indirect proof for the existence of embedded particles. The few reports on the synthesis of either metallic or oxidic nanoparticles in MOFs have mostly been performed with MOF-5; however some other MOFs have been studied as well. We shall therefore, now discuss the synthesis of nanoparticles in MOF-5 followed by their synthesis in other MOFs.

4.2 Metal Nanoparticles Inside MOF-5

In the first report on the synthesis of metal nanoparticles inside MOF-5, the formation of Pd, Cu and Au nanoparticles inside this framework was presented [59]. After loading with the corresponding precursors $[CpPd(\eta^3\text{-}C_3H_5)]$, $[CpCu(PMe_3)]$ or $[Au(CH_3)(PMe_3)]$, (see above) decomposition of the precursor to nanoparticles was achieved by either photolysis (UV radiation) or hydrogenolysis. Both, UV radiation and H_2 treatment, even at elevated temperatures, left MOF-5 unchanged, with controlled decomposition of precursor molecules *only*.

4.2.1 Pd@MOF-5

Palladium nanoparticles with a dimension of 1.4 nm were obtained by photolysis of $[CpPd(\eta^3\text{-}C_3H_5)]$ in MOF-5 at room temperature or below (with cooling) in the absence of additional hydrogen, leaving a perfectly intact MOF-5 matrix as confirmed by powder X-ray analysis and N_2 sorption measurements (see Fig. 9) [59]. The powder XRD of the corresponding sample shows an additional broad

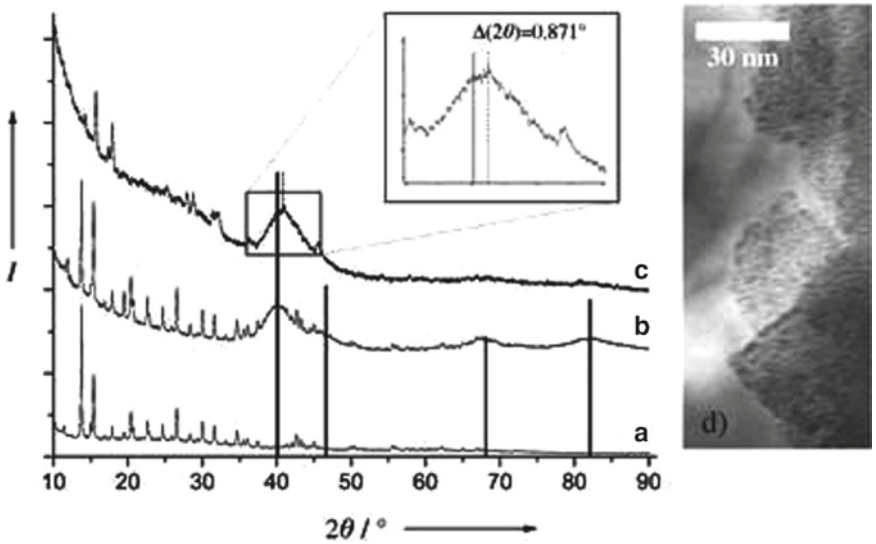

Fig. 9 Powder X-ray diffraction patterns of (**a**) MOF-5, (**b**) photolytically generated Pd@MOF-5, (**c**) Pd@MOF-5 generated by hydrogenolysis and (**d**) TEM picture of photolytically generated Pd@MOF-5 [59]. Copyright Wiley-VCH Verlag GmbH & Co. KGaA. Reproduced with permission

reflection (FWHM = 5.4°) at 2θ = 40.99° typical for nanocrystalline Pd particles. The size of the nanoparticles derived from TEM and PXRD data (Scherrer equation) is in good agreement with the diameter of the MOF-5 cavities (see above) hinting at nanoparticles embedded in the porous host. Treatment of the same precursor@MOF-5 composite with H_2 gas at −35°C led to Pd nanoparticles in the same size regime, here, however, the MOF-5 matrix appears to have lost its 2D long range order (see Fig. 9) Elemental analysis in both cases gave a metal loading of 35.6 wt% Pd.

In order to gain a more thorough insight into the particle distribution throughout the framework, a more detailed analysis of the photolytically synthesized Pd@MOF-5 was performed [74]. These results are illustrated in Figs. 10 and 11. Figure 10a shows a bright field TEM picture of a MOF-5 nanocrystallite with embedded Pd nanoparticles. The enlargement (Fig. 10b) clearly shows the Pd nanoparticles in a size range of 1–3 nm as darker spots, with the larger nanoparticles most probably located either close to the surface of the nanocrystallite or in a locally distorted environment in the inner core of the crystallite. From nanoparticle formation inside zeolitic materials it is known, that particles with a bigger size than the pore diameter can be formed inside the bulk of the matrix [75]. Note that, from the full width at half maximum (FWHM) of the Pd reflection in the PXRD of Pd@MOF-5 (Fig. 9) the particle size was calculated to be well below 3 nm. Evidently, the growth of the particles might cause a local distortion of the framework, allowing larger particles to grow. The selected area electron diffraction

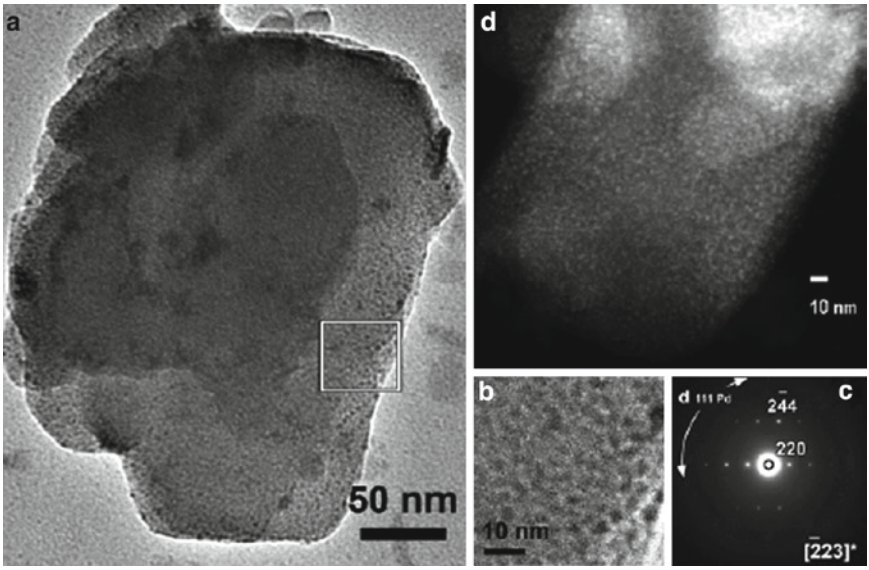

Fig. 10 Pd@MOF-5; (**a**) Bright field TEM image showing the Pd loaded framework. The crystal is faceted, indicating that the framework is still intact after loading; (**b**) Enlarged image of the region indicated (**a**) the particles have sizes ranging from 1 to 3 nm; (**c**) Diffraction pattern taken from a cubic Pd@MOF-5 crystal in [−223]* zone axis. A *weak ring* corresponding to the 111 planes of cubic Pd is also visible; (**d**) HAADF image of the Pd@MOF-5 material showing the Pd particles as *white spots*. Reproduced with permission from [74]. Copyright 2008 American Chemical Society

(SAED) pattern of the corresponding sample is given in Fig. 10c and confirms the intact structure of MOF-5 (sharp reflections) indicating that the crystallite is shown along the [−223] zone axis. In addition to the relatively sharp reflections of the host structure, a faint ring at 2.25 Å is also visible in the SAED pattern which is typical for the cubic spacing of Pd(111). This shows that the embedded particles exhibit the cubic Pd structure which is in agreement with the results from the PXRD analysis of the composite (Fig. 9). Figure 10d presents the result of a high-angle annular dark field scanning transmission electron microscopy (HAADF-STEM) measurement of the same material. The contrast in this type of image depends on both the thickness and the atomic number Z of the sample. Here, the heavier Pd nanoparticles appear as white dots within the MOF-5 framework. From this picture a close packing of the particles can be deduced. The 3D distribution of the Pd nanoparticles inside MOF-5 was examined by tomographical TEM measurements (Fig. 11), for which a 3D reconstruction of several TEM images of Pd@MOF-5 was performed. The TEM image of Pd@MOF-5 in Fig. 11a exhibits Pd nanoparticles in a range of 1–5 nm, however the larger particles here seem to be agglomerates of several smaller particles.

In tomographical TEM measurements, the resolution is usually rather low in order to avoid beam damage of the sample, and, therefore, smaller particles within the

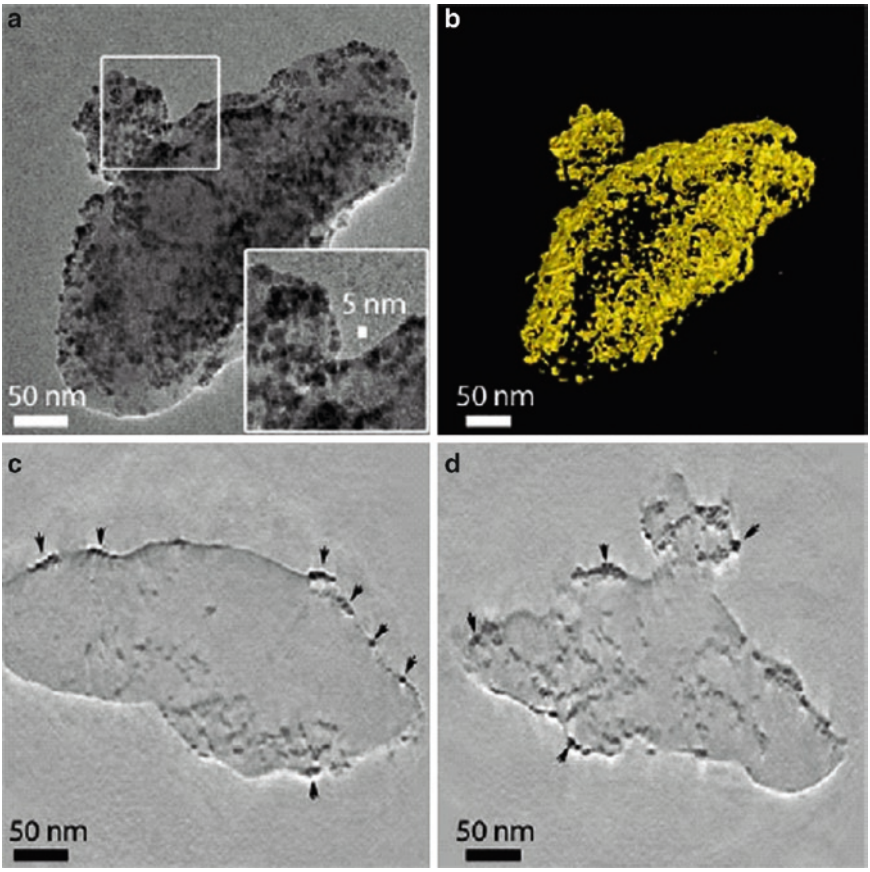

Fig. 11 (**a**) Bright field TEM image of a Pd@MOF-5. Inset; particles from 1 to 5 nm in diameter are present, some particles appear to have agglomerated; (**b**) Tomographically reconstructed Pd particles (matrix not imaged); (**c**) and (**d**) Slices through the tomographically reconstructed volume: the metallic particles are mostly imbedded inside the MOF-5 matrix. Reproduced with permission from [74]. Copyright 2008 American Chemical Society

areas of agglomerates cannot be resolved. The 3D tomographical reconstruction, however, clearly shows the rather uniform particle distribution throughout the framework (Fig. 11b). Inside the imaged MOF-5 matrix (specimen), the particles are in a size range of 1–3 nm (see above). At the surface of the specimen larger agglomerates are observed. Thus, the tomographical measurements provide a direct measure of the particle distribution throughout the framework. In the photolytically synthesized Pd@MOF-5, the particle distribution appears to be rather uniform, although some larger particle agglomerates at the surface of the MOF-5 crystallites can be detected. Another route to introducing Pd nanoparticles into MOF-5 was presented by Kaskel et al. [39–44]. Here, MOF-5 powder was loaded

with a solution of $[Pd(acac)_2]$ in $CHCl_3$ following standard recipes of the "incipient wetness technique." For this technique the volume of the solvent applied in the loading procedure is estimated from the free volume of the porous material used. The corresponding precursor molecules are then dissolved in this restricted amount of solvent and infiltrated into the porous material. Decomposition of the precursor was achieved by thermal treatment at 150–200°C or hydrogenolysis at 150–200°C. The metal loading was determined to be 1 wt% by elemental analysis and no additional reflections for Pd were observed in the PXRD of the composite. Due to the low metal loading, detection of the embedded Pd species and its chemical nature, whether fully reduced to Pd^0 nanoparticles or still some remaining Pd^{2+} species, was difficult. These aspects were not reported and discussed in detail by the authors. The BET surface area of the composite material was however reduced in comparison to the starting material, from 2,885 to 958 $g\,m^{-2}$ which is most probably due to the embedding of Pd nanoparticles. In another approach, Kaskel et al. also applied coprecipitation for the preparation of Pd in MOF-5 [76]. In this case, $Pd(NO_3)_2$ was directly added during the synthesis of the MOF, leading to Pd contents of 0.43–0.64 wt%. Again, no Pd reflections were observed in the corresponding PXRD data, although a slightly reduced surface area was observed. The detection of the location and the nature of imbedded metal species in MOF-5 remains a particular challenge, especially when the corresponding metal content is rather low. Here the detection limit of most analytic techniques obviously anticipates a detailed examination. However, our study on Pd@MOF-5 at a high metal loading of 35.6 wt% shows the general ability of MOF-5 to host metal nanoparticles.

4.2.2 Ru@MOF-5

In order to study the stabilizing property of MOF-5 in comparison to the surfactant approach in non aqueous colloid chemistry of metal particles, the system Ru@MOF-5 was selected as a target [64]. The synthesis and characterization of Ru colloids starting from [Ru(cod)(cot)] in solution is well reported in the literature [77–79].

Therefore, this species is a well suited model system for investigation inside MOFs. With a preparation method similar to the one described above, Ru nanoparticles in MOF-5 were obtained. Thus, [Ru(cod)(cot)] can be introduced into the porous $[Zn_4O(bdc)_3]$ and hydrogenolysis at lower temperatures and H_2 pressure lead to coordination of {Ru(cod)} species to part of the *bdc* linkers as a side reaction to Ru nanoparticle formation. "Pure" Ru@MOF-5 was obtained by hydrogenolysis at 150°C, 3 bar H_2, 48 h, with an Ru content of 31.5 wt%. As in the case of higher Pd loadings in MOF-5, an additional reflection for Ru is observed in the PXRD of the composite. Here also the low angle region of the PXRD was investigated. The change of the reflection intensities was not as pronounced as in the case of the intact precursor due to only a fraction of all MOF cavities occupied by Ru particles [64]. Given an Ru content of 31.5 wt% and based on the fact

that Ru nanoparticles in the size regime of the MOF-5 cavities are likely to consist of~140–150 atoms, only 2% of all MOF-5 cavities would be filled with Ru particles. The corresponding TEM micrographs reveal small Ru nanoparticles of 1.5–1.7 nm, matching the typical MOF-5 pore diameter, distributed over the porous matrix without any bigger agglomerates at the surface (Fig. 12). The SAED pattern of hexagonal Ru could be detected, and the distribution of the Ru nanoparticles was examined with tomographical TEM measurements which are illustrated in Fig. 13 [74]. Figure 13a shows a more or less uniform particle distribution of the Ru nanoparticles throughout the MOF-5 nanocrystallite. In contrast to this, the tomographical

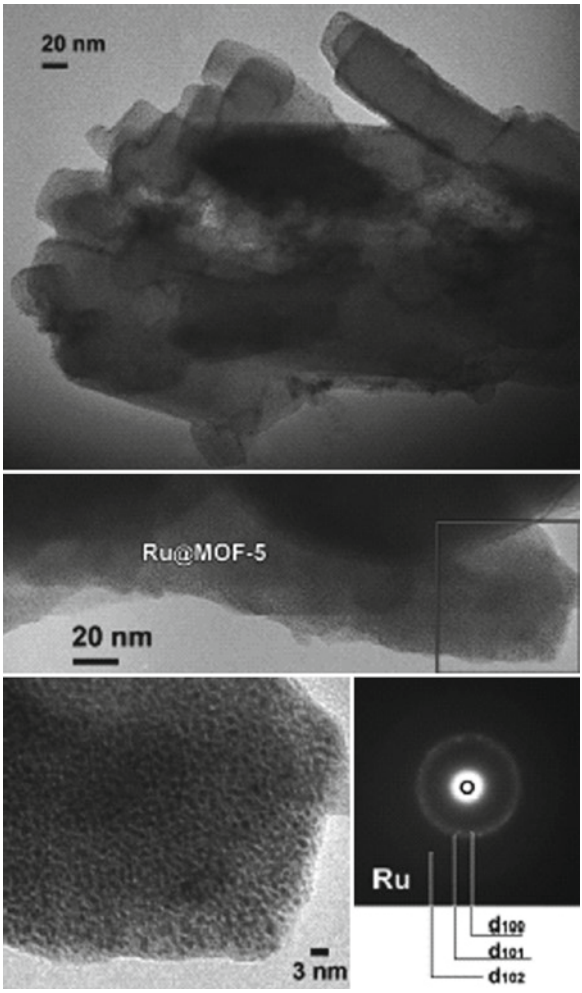

Fig. 12 TEM pictures of Ru@MOF-5 with a corresponding SAED pattern for the embedded Ru nanoparticles. Reproduced with permission from [64]. Copyright 2008 American Chemical Society

3D reconstruction (Fig. 13b) shows that most of the particles are in fact located at the outer domains of the investigated MOF-5 specimens with a maximum penetration of 20 nm, and only some particles are located in the core of the MOF-5 crystallites. This is in contrast to the results from the tomographical TEM measurements of Pd@MOF-5 (Fig. 11), where a more or less uniform particle distribution was observed. Obviously, the preparation technique has a great impact on the particles distribution. The photolytically synthesized Pd@MOF-5 shows a more uniform particle distribution than the material Ru@MOF-5, which was obtained by thermally activated hydrogenolysis over a long period of time. In the case of Ru@MOF-5,

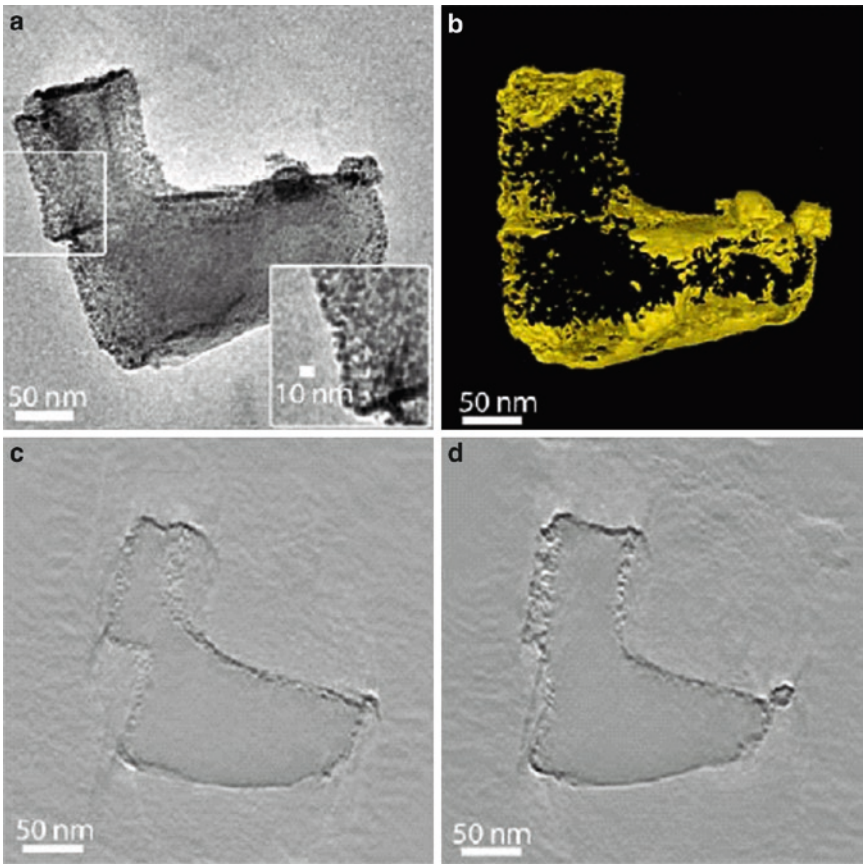

Fig. 13 (**a**) Bright field TEM image of a Ru loaded MOF. Inset; particles from 1 to 5 nm in diameter are present, the matrix appears to be densely packed; (**b**) Tomographically reconstructed Ru particles (matrix not imaged) Some overlapping of the particles is present due to diffraction contrast; (**c**) and (**d**) Slices through the tomographically reconstructed volume: the metallic particles are not completely imbedded in the inner core of the MOF-5 matrix. Most particles are positioned at the surface of the matrix, or close to the surface (up to approximately 20 nm deep). Reproduced with permission from [74]. Copyright 2008 American Chemical Society

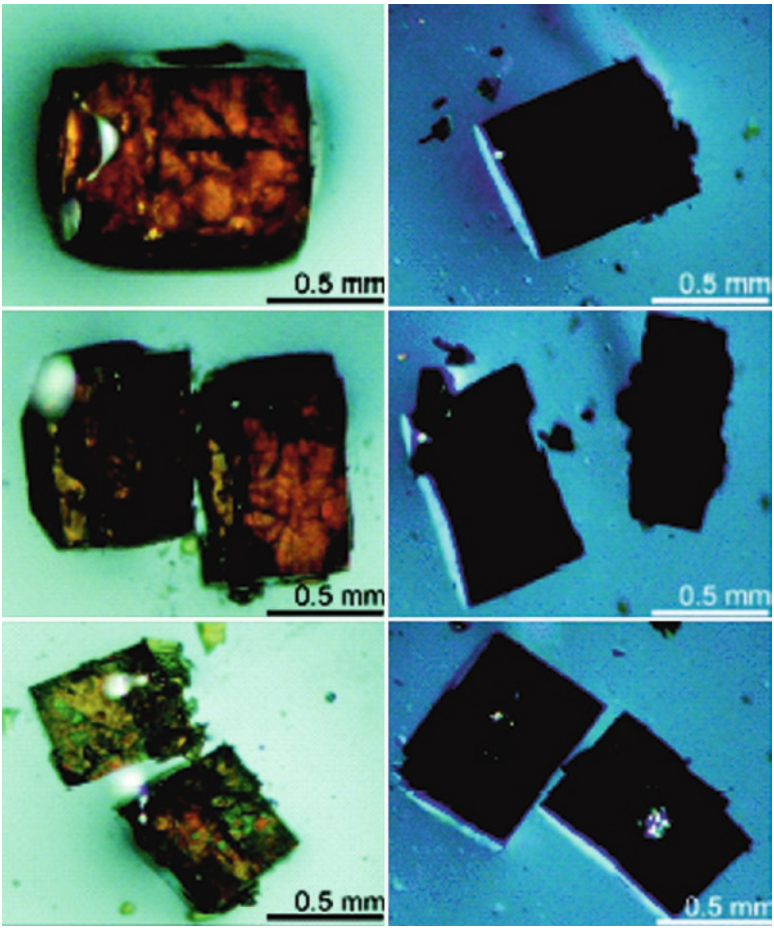

Fig. 14 Images of millimeter-sized MOF-5 crystals after loading with [Ru(cod)(cot)] before (*left*) and after (*right*) treatment with H_2. The presented crystals on the *left* and the *right* side stem from the same loading experiment. One of them (*right*) was then treated with H_2. In order to show the macroscopically uniform distribution of the precursor and the Ru nanoparticles after hydrogenolysis, the crystals were cut (*middle*) and turned to examine the cross section (*bottom*). Reproduced with permission from [64]. Copyright 2008 American Chemical Society

presumably an autocatalytical process starting at the surface of the MOF-5 crystallites leads to a segregation of the particles to the interfaces of the MOF-5 microcrystals in a powder sample. Loading a MOF-5 single crystal however, the distribution of [Ru(cod)(cot] precursor molecules is rather uniform as can be observed by the light microscopic image in Fig. 14. Also the Ru nanoparticle distribution on the macroscopic scale appears to be uniform, when such a single crystal is exposed to the hydrogenolysis. However, the detailed investigation by TEM on the nanoscale

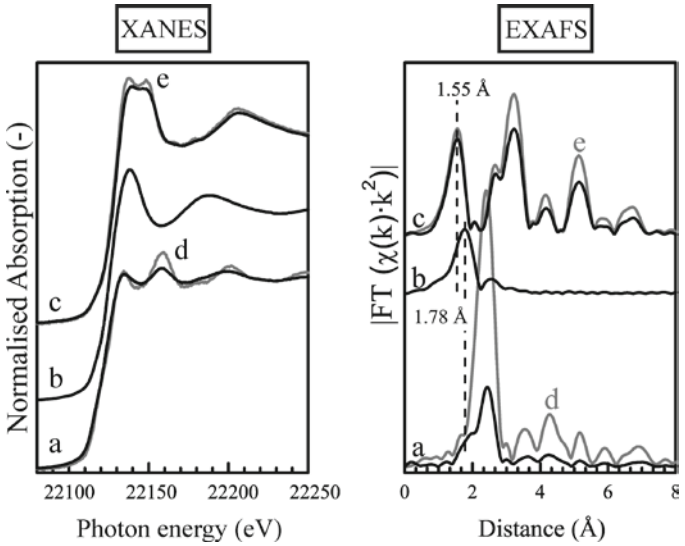

Fig. 15 XANES (*left*) and EXAFS (*right*) of (**a**) Ru@MOF-5, (**b**) [Ru(cod)(cot)@MOF-5, (**c**) Ru–ox@MOF-5, (**d**) Ru foil and (**e**) RuO_2. All data were recorded at liquid nitrogen temperature. Reproduced with permission [64]. Copyright 2008 American Chemical Society

reveals quite the opposite, with Ru nanoparticles mostly located close to the outer surface of the imaged specimen.

XAS measurements were performed on the Ru@MOF-5 powder material to give additional insights into host–particle interactions. The X-ray absorption near edge structure (XANES) of Ru@MOF-5 is indicative of metallic ruthenium. The curves of Ru@MOF-5 and the reference Ru foil overlap to a large degree and the edge shift excludes oxidation of the Ru nanoparticles (Fig. 15a). The EXAFS of Ru@MOF-5 is typical for small Ru nanoparticles with a small amplitude in the FT curve for the first Ru shell when compared to the Ru foil (Fig. 15b). Interestingly, a small shoulder is visible in the EXAFS of Ru@MOF-5 at 1.78 Å which can be assigned to a Ru–C interaction most probably from interaction of the Ru nanoparticles and the *bdc* linkers. This is indirect proof for the Ru nanoparticles being indeed located *inside* the MOF-5 matrix. This example nicely shows the combination of different methods in order to investigate the location of nanoparticles inside MOFs. The framework–particle interaction was studied also by static ^2H solid state NMR of surface-bound hydrides on Ru nanoparticles inside MOF-5. A remarkably high mobility was found, even exceeding the one of surface hydrides on Ru colloids. This suggests a rather weak framework–particle interaction superior to that of other common porous solids which also explains the particle distribution within the framework observed by tomographical TEM measurements. Presumably, the surface of nanoparticles embedded in MOF-5 is readily accessible to reagents, e.g., in catalytic applications.

4.2.3 Cu@MOF-5 and Au@MOF-5

In addition to the already discussed metal@MOF-5 composites Pd@MOF-5 and Ru@MOF-5, the synthesis of copper and gold nanoparticles in MOF-5 has also been investigated. As for the synthesis protocols discussed above, these materials were obtained by hydrogenolysis of [$CpCuPMe_3$)] [51,72] or [$CpCu(CN^tBu)$] [80] and [$Au(CH_3)(PMe_3)$] [59] as precursors in MOF-5 at elevated temperatures. Figure 16 shows the PXRD patterns of the parent MOF-5 as well as the ones of the Cu precursors in MOF and Cu@MOF-5 synthesized from these composites. The characteristic reflections of the MOF-5 host are retained in all cases. The structural quality of the Cu@MOF-5 composite derived from [$CpCu(CN^tBu)$]@MOF-5 appears to be better than the one of the material derived from [$CpCu(PMe_3)$]@MOF-5. This effect may be due to the interaction of the PMe_3 ligand with the MOF-5 matrix [80]. From PXRD and TEM measurements, the size of the Cu nanoparticles was determined to be in a range of 1–3 nm (see discussion above) with a metal loading of 10–11 wt%. In this case tomographical TEM measurements to determine the particle distribution inside the MOF-5 host were not performed.

In contrast, TEM and PXRD data of Au@MOF-5 show polydispersed Au particles in a size range of 5–20 nm (see Fig. 17), with a metal loading in Au@MOF-5 determined to be 48 wt%. The gold particles appear to interact more weakly with the host matrix than the Pd, Ru and Cu particles and thus larger agglomerates are formed possibly by diffusion of the particles to the outer surface.

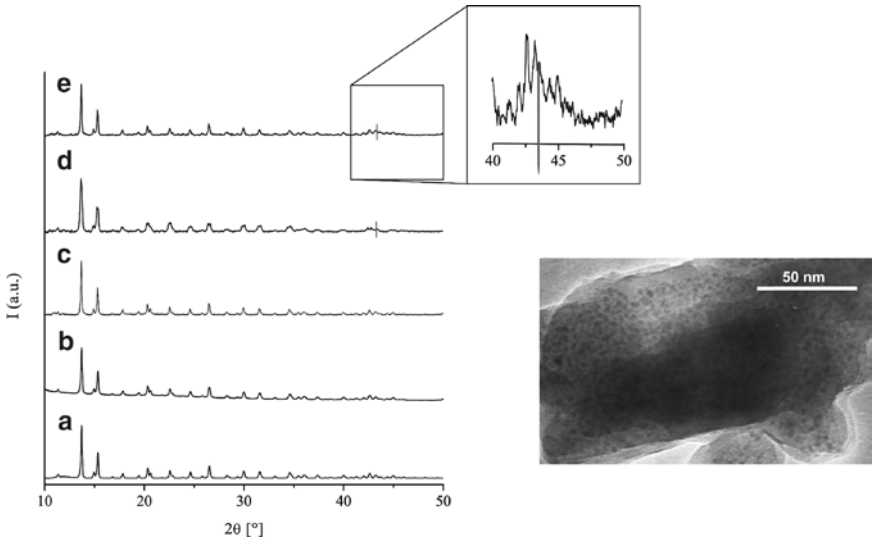

Fig. 16 Powder X-ray diffraction patterns of (**a**) pure, activated MOF-5, (**b**) [$CpCu(PMe_3)$]@MOF-5, (**c**) [$CpCu(CN^tBu)$]@MOF-5, (**d**) Cu@MOF-5 (derived from [$CpCu(PMe_3)$]@MOF-5) (**e**) Cu@MOF-5 (derived from [$CpCu(CN^tBu)$]@MOF-5). TEM image of Cu@MOF-5 (derived from [$CpCu(PMe_3)$]@MOF-5). Reproduced with permission [80]. Copyright 2008 American Chemical Society

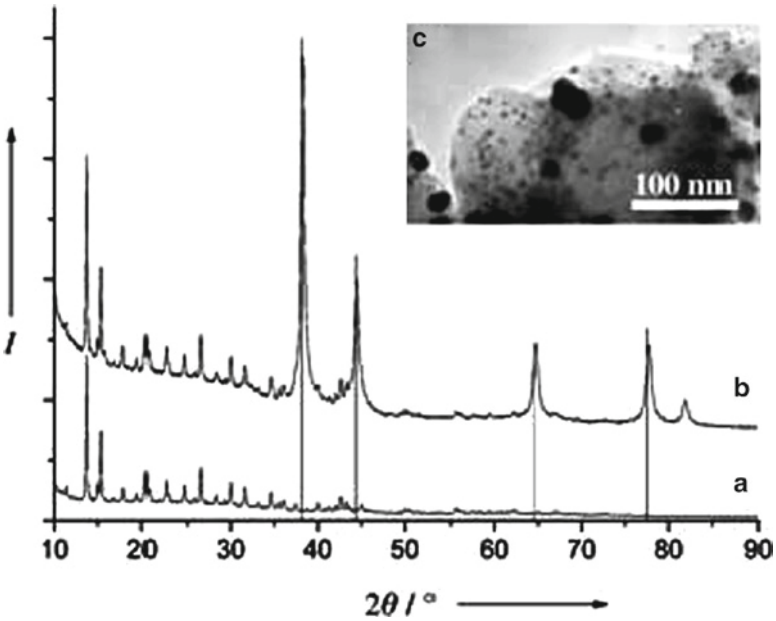

Fig. 17 Powder X-ray diffraction patterns of (**a**) MOF-5, (**b**) Au@MOF-5 and (**c**) TEM picture of Au@MOF-5 [59]. Copyright Wiley-VCH Verlag GmbH & Co. KGaA. Reproduced with permission

Similar observations have been made for the loading of mesoporous silica in which Au and Ag nanoparticles grow larger than the pore diameter of the host, presumably due to a destructive growth mechanism of the embedded particles [81–83]. We have already discussed the rather weak interaction between the particles and the host framework for Ru@MOF-5. From the TEM pictures of the Pd, Ru and Cu nanoparticles in MOF-5 it can be deduced that they are mostly located inside the framework even though few nanoparticles exhibit a size larger than the MOF-5 pore diameter. In this case a local distortion of the porous host allows particles to grow slightly larger than the actual pore size. In order to create a stronger interaction between the host and the embedded particles, several approaches appear possible. The functionalization of the MOF-5 linkers with –OH, –OR, –SH or $–NH_2$ groups is one possible strategy to bind the embedded particles to the framework. Another approach is the embedding of metal oxide species in the MOF matrix prior to the embedding of the nanoparticles to increase the interaction between the host and the metal nanoparticles. In combination with metal nanoparticles, metal oxide species in MOFs are known to have a promoting effect on catalytical properties of the embedded metal nanoparticles as seen in Cu/ZnO composites in methanol catalysis [84–87]. In addition, nanosized metal oxide species such as ZnO or TiO_2 embedded in MOF could enhance the semiconducting properties of MOF-5 [20,21].

4.3 Metaloxide@MOF and Metal/Metaloxide@MOF

In this section we will refer to the formation of metal oxide and metal/metal oxide species in MOF-5 similar to the formation of metal nanoparticles@MOF-5. After infiltration of precursor molecules, oxidation of the precursor molecules to oxide species by O_2 gas is performed. However classical sol–gel chemistry might be another synthetic strategy to yield oxide species inside MOFs and will surely be investigated in the future. Due to the sensitivity of MOF-5 towards moisture however, a sol–gel approach is not feasible. The sol–gel chemistry inside MOFs requires water stable structures. We have reported the synthesis of Cu/ZnO species in MOF-5, the preparation of nanometer sized ZnO species in MOF-5 and the subsequent introduction of Cu nanoparticles [80]. $ZnEt_2$ was used as a ZnO precursor and was adsorbed inside MOF-5 and then converted to ZnO species by either exposure to O_2 gas (dry method) or by very careful hydrolysis (wet method), followed by annealing at 250°C. ^{17}O labeling studies using $H_2{}^{17}O$ revealed that neither the *bdc* linkers nor the central oxide ion of the Zn_4O unit exchange oxygen atoms/ions with the imbedded ZnO species [80]. Depending on the preparation conditions, Zn contents from 10 to 35 wt% were introduced in MOF-5. Results from PXRD, TEM, UV–VIS and ^{17}O MAS-NMR spectroscopy gave evidence for a largely intact MOF-5 matrix with imbedded ZnO nanoparticles <4 nm (see Fig. 18).

Langmuir surface areas of the composite gave values of 900 $m^2 g^{-1}$ (wet method) and 1,750 $m^2 g^{-1}$ (dry method) which shows the advantage of the dry method, leaving a remarkably high surface area at a Zn loading of 35.5 wt%. The corresponding TEM micrographs reveal the typical faceted MOF-5 nanocrystallites. However, due to the low contrast of the ZnO in the Zn-based MOF matrix, the single particles could not be detected. In addition to the synthesis of ZnO@MOF-5, TiO_2@MOF-5 was obtained by the oxidation of $Ti(OiPr)_4$ inside the MOF cavities [88]. The resulting metal oxide aggregates are presumably quite small and neither showed reflections in the PXRD nor in the SAED. Attempts to synthesize CuO or Cu_2O species in MOF-5 by oxidizing the composite Cu@MOF-5 with O_2 led to a complete collapse of the framework as indicated by PXRD [80]. Yet, soft oxidation of the embedded Cu nanoparticles with N_2O yields core-shell Cu_2O/Cu nanoparticles inside the framework with the host matrix remaining completely unchanged. The oxidation is completely reversible and upon treatment with H_2 gas Cu_2O/Cu@MOF-5 is fully re-reduced to Cu@MOF-5 [80]. Cu/ZnO@MOF-5 was obtained by gas phase loading of ZnO@MOF-5 with [CpCuL] (L = PMe_3, CN^tBu) followed by hydrogenolysis. Here, a Cu loading of 1.4 wt% together with a ZnO loading of 9.9 wt% was obtained. The composite exhibited a surface area of 920 $m^2 g^{-1}$ indicating an intact host matrix. In this case, the order of introduction of the different nano species is a crucial point. Although both precursors of ZnO and Cu nanoparticles were infiltrated in the MOF simultaneously as unchanged molecules, the simultaneous conversion by pyrolysis, photolysis or hydrogenolysis of both to Cu/ZnO@MOF-5 failed and

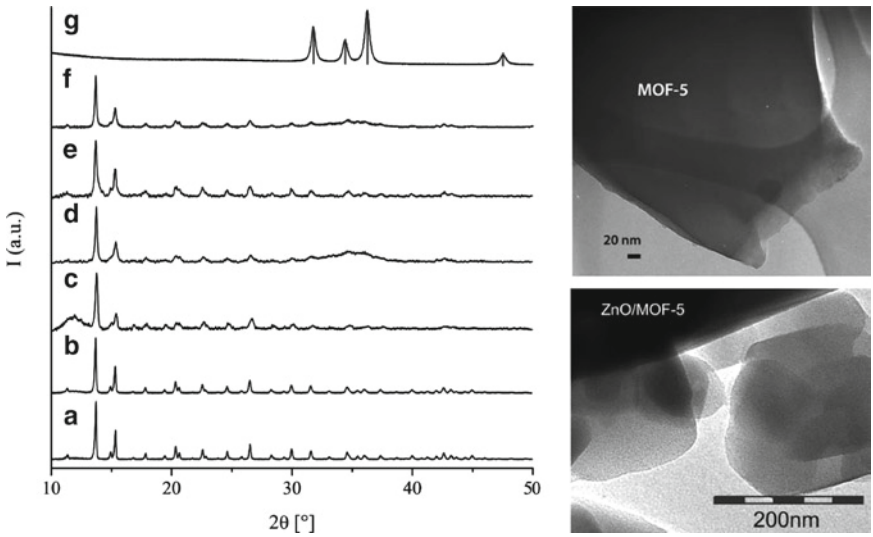

Fig. 18 *Left*: Powder X-ray diffraction patterns of MOF-5 (**a**), [$ZnEt_2$]@MOF-5 (**b**), as ZnO@MOF-5 (as synthesized by the wet method) (**c**), ZnO@MOF-5 (after annealing and derived by the wet method) (**d**), as ZnO@MOF-5 (as synthesized by the dry method) (**e**), ZnO@MOF-5 (after annealing and derived by the dry method) (**f**) and ZnO-reference sample obtained from controlled hydrolysis of $ZnEt_2$ and annealing in air (**g**). The positions of the characteristic reflections of hexagonal ZnO are marked. *Right*: TEM images of unloaded MOF-5 (a) and ZnO@MOF-5 (f, after annealing and derived by the dry method). Reproduced with permission [80]. Copyright 2008 American Chemical Society

led to the collapse of the host matrix. Therefore, the Cu precursor had to be introduced after the formation of the ZnO species in MOF-5. Below we will discuss the catalytic properties of the obtained composite Cu/ZnO@MOF-5.

4.4 Other Frameworks and Other Loading Techniques

Due to its easy accessibility and photochemical as well as thermal stability MOF-5 has been the typical study case for nanoparticle@MOF synthesis and characterization. However, a few studies of other frameworks are known as well and are summarized in the following.

4.4.1 Noble Metal Particle Formation at Redox-Active Frameworks

Suh et al. studied the nanoparticle formation in MOFs using metal salts as precursors which are reduced to form metal clusters by a special redox-active framework

[89–91]. Silver nanoparticles of ~3 nm are formed when the MOF $[\{Ni(C_{10}H_{26}N_6)\}_3(bpdc)_3]\cdot 2C_5H_5N\cdot 6H_2O$ (bpdc = 4,4′-biphenyldicarboxylate; Fig. 19) is immersed in a methanolic solution of $Ag(NO_3)$. The reaction proceeds stoichiometrically with a relation of a ration of Ni^{2+}(in the host): Ag^+ of 1:1. The host framework remains unchanged upon oxidation of its Ni-centers from Ni^{2+} to Ni^{3+}. Due to the positive charge of the MOF during the redox reaction, however, NO_3^- ions are adsorbed in the framework channels as well. The size of the Ag nanoparticles (3 nm) exceeds the window size of the host framework of 7.3 Å (Fig. 20), which might be due to diffusion of the particles to the framework's surface [89]. Similarly, in a second report Suh et al. presented the synthesis of Ag and Au nanoparticles by the redox reaction of $Ag(NO_3)$ or $HAuCl_4$ with the 2D framework $\{[Ni(cyclam)]_2[BPTC]\}_n\cdot 2nH_2O$

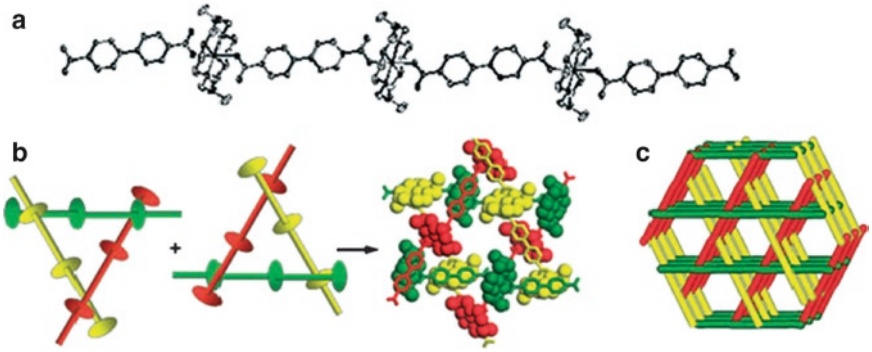

Fig. 19 X-ray structure of $[\{Ni(C_{10}H_{26}N_6)\}_3(bpdc)_3]\cdot 2\ C_5H_5N\cdot 6\ H_2O$. (**a**) Structure of the linear coordination polymer. (**b**) Double network of threefold braids where macrocycle grooves are created by $bpdc^{2-}$ ligands. (**c**) View showing the stacking of the linear chains to generate 1D channels [89]. Copyright Wiley-VCH Verlag GmbH & Co. KGaA. Reproduced with permission

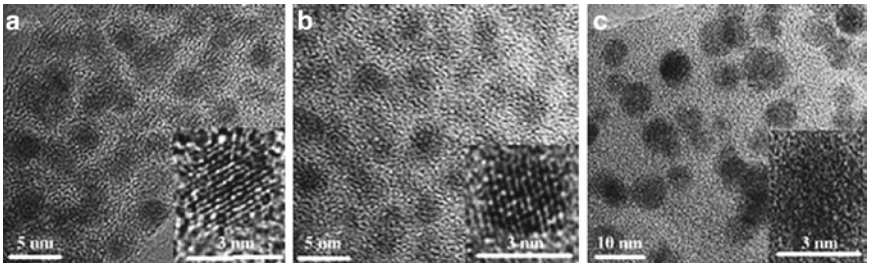

Fig. 20 HRTEM images of $[\{Ni(C_{10}H_{26}N_6)\}_3(bpdc)_3]$ after immersion in methanolic $Ag(NO_3)$ solution at room temperature for (**a**) 10 min, (**b**) 18 h and (**c**) after removal of the host by heating the solid of (**b**) in dioctylether solution [89]. Copyright Wiley-VCH Verlag GmbH & Co. KGaA. Reproduced with permission

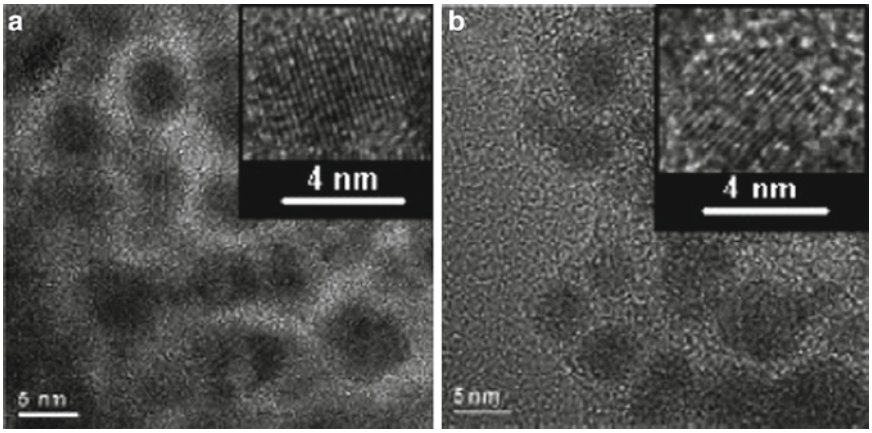

Fig. 21 HRTEM images of Ag nanoparticles formed by immersion of $[Ni(cyclam)]_2[BPTC]\}_n \cdot 2_n H_2O$ in the EtOH solution of $AgNO_3$ (1.3×10^{-1} M) at room temperature (**a**) for 5 min and (**b**) for 16 h [90]. Copyright Wiley-VCH Verlag GmbH & Co. KGaA. Reproduced with permission

(cyclam = 1,4,8,11-tetraaza-cyclotetradecane and BPTC = 1,1´-biphenyl-2,2´,6,6´-tetracarboxylate) [90].

Ag nanoparticles of 4 nm and Au nanoparticles (Fig. 21) of 2 nm are obtained which exceed the void size between two layers in the framework. As in the case above, the authors assume particle diffusion to the surface of the framework as a reason for this finding. In addition, Suh et al. reported Pd nanoparticle synthesis in the MOF $[\{Ni(cyclam)]_2(mtb)\}_n]\cdot 8n\ H_2O \cdot 4n$ DMF (mtb = methanetetra-benzoate) from $Pd(NO_3)_2$ solution in acetonitrile [91]. The presumably stoichiometric reaction between the Ni^{II} centers of the framework and the Pd salt, gives Pd^0 and Pd^{II} coexisting in the framework as determined by XPS measurements. TEM analysis reveals that again the size of the obtained Pd nanoparticles exceeds the size of the MOF channels. In this case, the authors state that Pd nanoparticles were already spontaneously formed from the solution of $Pd(NO_3)_2$ in MeCN [91]. In all examples of metal nanoparticles formed at the redox-active MOFs, the sizes of the obtained nanoparticles largely exceed those of the host channels (i.e., 3 nm particles in a framework with 7.3 Å pore diameter). No TEM tomographical measurements have been reported for these composites. Also, it is not clear whether the redox reaction requires a penetration of the noble metal salt into the MOF or whether these reactions occur only at the surface. It is not really clear whether the particles are actually still located in the framework ("outer surface") or indeed outside. From the presented TEM pictures it cannot really be ruled out that at least some of the larger particles are located outside the framework. For MOF-5 we have already discussed the rather low interaction between the framework and embedded particles which might allow the diffusion of the particles out of the host matrix. This might also be the case for the redox-active MOFs.

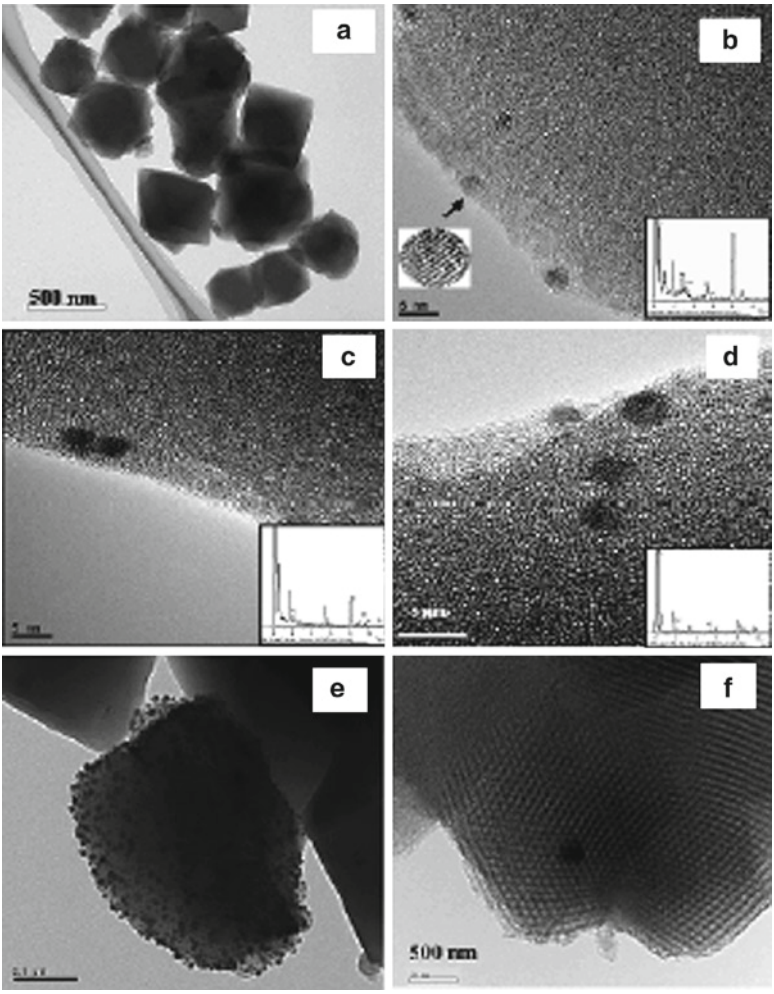

Fig. 22 TEM images of as synthesized MIL-101 and precious metal immobilized EDMIL-101. (**a**) as synthesized MIL-101, (**b**) Pd/ED-MIL-101, (**c**) Au/ED-MIL-101, (**d**) Pt/EDMIL-101, (**e**) Pd- impregnated MIL-101 and (**f**) Pd/APS-SBA-15. Insets are EDX profiles of impregnated precious metal nanoparticles [92]. Copyright Wiley-VCH Verlag GmbH & Co. KGaA. Reproduced with permission

4.4.2 Grafting of Metal Nanoparticles Inside MOFs

A method known from nanoparticle synthesis in silica materials was introduced very recently to direct the loading with metal precursors and in parallel to reduce the problems resulting from the rather low interaction of the host materials with

embedded particles. The synthesis of Pd, Pt and Au nanoparticles inside chromium based MIL-101 was reported by Férey et al. [92].

A subsequent treatment with HCl resulted in the formation of ammonium groups inside the cavities in order to facilitate ionic interactions with $[PdCl_4]^{2-}$, $[PtCl_6]^{4-}$ or $[AuCl_4]^-$ as carrier species for the noble metal component. Finally, the adsorbed anionic noble metal complex was reduced with $NaBH_4$. Again, the particle formation has no influence on the crystallinity of the host framework and no additional Bragg peaks are visible in the PXRD patterns. This is possibly due to the surprisingly low metal loading of about 1 wt%. TEM analysis reveals particle sizes of 2–4 nm matching the pore dimensions of MIL-101 (2.4 and 3.9 nm). However, larger particles outside the framework were also detected by TEM which might be due to a leaching process during the reduction step of the metal salt (Fig. 23). The grafting of the MIL-101 frameworks has a great effect on the interaction between the framework and the embedded particles. Through grafting of the framework with functional amine groups, it was possible to obtain Au nanoparticles embedded inside the framework. As discussed above, Au nanoparticles might otherwise readily diffuse out of the framework to form larger agglomerates. The overall metal content of Pd, Pt and Au in MIl-101 is rather low, so it will be interesting to see in future whether an increased loading can be obtained and what effect it will have on the particle sizes in the MIL materials. In addition, synthesis of Pd@MIL-101 was also performed using the "incipient wetness technique" by Kaskel et al. [93]. Using a similar procedure to that published previously on the loading of MOF-5 [51], Pd nanospecies in MIL-101 at rather low Pd content (1 wt%) were obtained. As in the previous work of the same group [51], no additional Bragg reflections for palladium were observed in the corresponding PXRD

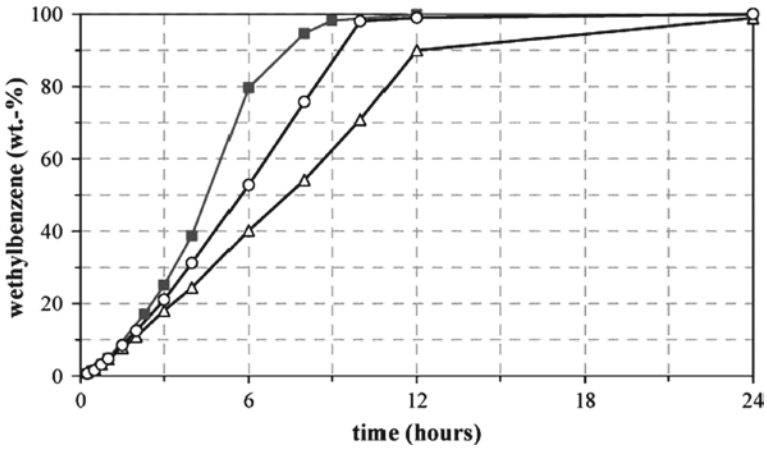

Fig. 23 Ethylbenzene formation with different Pd supported catalysts. *Filled square* represents Pd@MOF-5 (1 wt%), *open circle* represents Pd/Norit A (1 wt%) and open *triangle* represents Pd/C (purchased from Aldrich,1 wt%[51]. Reproduced with permission of The Royal Society of Chemistry

of Pd@MIL-101. The results from N_2 and H_2 sorption measurements, however, indicate the loading of the pores in MIL-101.

4.5 Applications of Nanoparticles Loaded MOFs in Catalysis

Most of the examples of metal@MOFs and metaloxides@MOFs discussed up to now have been synthesized in order to obtain novel kinds of supported nanoparticles with potentially advantageous properties for applications in catalysis. The catalytic properties of the composite materials Pd@MOF-5 and Cu@MOF-5 were among the first to be tested. The Pd@MOF-5 composite that was obtained by the gas phase loading/photolysis synthetic protocol (35.6 wt% Pd) showed moderate activity in catalysis of hydrogenation of cyclooctene [59]. The Pd@MOF-5 (1 wt%) synthesized by the "incipient wetness technique" from [$Pd(acac)_2$] was tested as catalyst in hydrogenation of styrene, 1-octene and *cis*-cyclooctene, and exhibited a slightly higher catalytic activity than Pd supported on activated carbon (Pd/Norit A; Fig. 23) [51].

The observed enhanced catalytic performance of Pd@MOF-5 (1 wt%) in comparison to Pd/Norit A (1 wt%) and Pd@MOF-5 (35.6 wt%) [59] is due possibly to the higher dispersion and accessibility of the active Pd sites in this sample. Also, Pd@MOF-5 was tested in hydrogen adsorption revealing a capacity of up to 1.86 wt% (at 77 K, 1 bar) clearly exceeding the value of Pd-free MOF-5 (1.32 wt% at 77 K, 1 bar) by about 40%. The material Pd@MOF-5 material obtained from coprecipitation [76] was also tested in hydrogenation catalysis of ethyl cinnamate, revealing an activity twice as high as the one of Pd supported on activated carbon. Again, the higher performance was attributed to the higher dispersion and better accessibility of the palladium; however, the actual microstructure of the catalyst is still unknown. From N_2 measurements of the composite material after subsequent catalytic test reactions, however, it was found that the Pd is most probably bound to the outer surface of the MOF-5 crystals. Therefore the as prepared composite might be less stable in prolonged catalytic runs than a sample with the Pd located in the MOF-5 pores. The Pd loaded MIL-101 composite was tested in catalysis of the Heck reaction of acrylic acid with iodobenzene. Its activity is comparable to that of commercially available Pd/C catalysts [92]. Kaskel et al. also performed catalytic test reactions of the composite Pd@MIL-101 [93]. The material exhibited a higher catalytic activity in the hydrogenation of styrene and octane than Pd@MOF-5. Furthermore, sustained activity in gas phase hydrogenation of acetylene/ethylene mixtures was found. The work of Kaskel et al. and Férey et al. show that for distinct catalytic applications, "incipient wetness" loading or solution loading in general might be more suitable than gas phase loading, since the metal content of the resulting metal@MOF composite can be controlled more readily. However other applications, e.g., methanol synthesis, demand a high metal (Cu) content of a catalyst sample. Here, the gas phase loading may be more advantageous, since comparably high metal loadings can be obtained rather straightforwardly. Accordingly,

the composite Cu@MOF-5 [59] was tested in methanol catalysis from synthesis gas (H_2/CO/CO_2) and showed some catalytic activity, matching the performance of Cu/ZnO@MCM-41 [94]. This is surprising since the promotion of Cu by ZnO_x species is usually essential for catalytic activity in methanol synthesis [80]. Apparently, in Cu@MOF-5 this is not necessary or provided in a novel form by the zinc carboxylate based host material MOF-5. A significant decomposition of Cu@MOF-5 during the catalytic test reactions to yield promoting ZnO has been ruled out by characterization of the used catalyst. In order to study the influence of additional ZnO species as a promoter for Cu@MOF-5, the Cu/ZnO@MOF-5 system discussed above was also tested as a catalyst for methanol synthesis. The material expectedly showed enhanced catalytic activity peaking at about 60% of an industrial reference catalyst [80]. With a comparably very low Cu loading of only 1.4 wt%, obviously a superior interfacial contact between the Cu and ZnO nano species must exist. However, the MOF-5 host material collapsed after several hours under catalytic conditions, leading to poor final activities. The same effect was found for the catalytic test reaction of Ru@MOF-5 (oxidized) in alcohol oxidation, although at the beginning of the test run, some conversion is observed [64]. Upon prolonged reaction time, the framework collapsed. These observations are attributed to the instability of MOF-5 against water, and water is a by-product in many oxidation reactions. Due to its sensitivity to water, MOF-5 appears to be less suitable as a support material in catalytic reactions that demand or release water. Yet, the presented results are encouraging and show the general potential of MOFs as support matrices in catalytic reactions. Beside the zinc carboxylate MOFs, other, more stable structures will be surely investigated in more detail in the future.

5 Conclusion

Different preparative approaches to forming nanoparticles inside MOFs have been reviewed herein. As for other porous materials, the characterization of the embedded particle and its location *in* or *outside* the framework is always a challenge. To date, nanoparticles with MOF-5 are still the most investigated systems. However, these results have been transferred to MOF-177, [62,63] HKUST-1 [38] and [Zn(bdc)(dabco)]. [38] It was found that the embedded particles interact very weakly with the host matrix such that, in the case of Au@MOF-5 large nanoparticles are formed outside the framework. The sizes of embedded Pd, Ru and Cu particles have been found to be in the range between 1–3 nm, which accounts for at least a fraction of the nanoparticles, exhibiting sizes that exceed those of the MOF-5 cavities (1.5 nm). Nevertheless, even the larger nanoparticles (>1.5 nm) are located inside the MOF-5 host matrix, most probably in a locally distorted environment, as seen in the case of Pd@MOF-5, in particular. Furthermore, nanoparticle distribution is obviously dependent on the synthesis procedure applied. Autocatalytic hydrogenolysis can lead to an agglomeration of particles at the outer surface of MOF-5 due to diffusion limitations of the reactive gas and the mobility of the included organometallic precursors.

In all examples, tomographical TEM measurements are clearly the most potent tool for the direct imaging of the embedded particles and for studying their location inside the host matrix. The usual 2D TEM pictures can present misleading results. Catalytic tests of the embedded Cu and Pd nanoparticles (and Ru nanoparticles) show the potential of MOFs to act as host materials for functional nanoparticles. Enhanced hydrogen storage capacity was measured for Pd@MOF-5 (1 wt%). However, MOF-5 is rather sensitive to water and moist air which limits its application as a host matrix. The results can, however, be clearly transferred to other nanoparticle@MOF composites that are more promising for industrial applications. Studies on nanoparticle synthesis in other MOFs have already been published and are very likely to be extended in the future. Host frameworks with a high temperature and chemical stability will surely be addressed in upcoming investigations.

References

1. Hoskins BF, Robson R (1989) J Am Chem Soc 111:5962
2. Hoskins BF, Robson R (1990) J Am Chem Soc 112:1546
3. Abrahams BF, Hoskins BF, Michail DM, Robson R (1994) Nature 369:727
4. Venkataraman D, Gardner GB, Lee S, Moore JS (1995) J Am Chem Soc 117:11600
5. Gardner GB, Venkataraman D, Moore JS, Lee S (1995) Nature 374:792
6. Li H, Eddaoudi M, O'Keeffe M, Yaghi OM (1999) Nature 402:276
7. Subramanian S, Zaworotko MJ (1995) Angew Chem Int Ed 34:2127
8. James SL (2003) Chem Soc Rev 32:276
9. Yaghi OM, O'Keeffe M, Ockwig NW, Chae HK, Eddaoudi M, Kim J (2003) Nature 423:705
10. Chae HK, Siberio-Pérez DY, Kim J, Go Y, Eddaoudi M, Matzger AJ, O'Keeffe M, Yaghi OM (2004) Nature 427:523
11. Côté AP, Benin AL, Ockwig NW, O'Keeffe M, Matzger AJ, Yaghi OM (2005) Science 310:1166
12. El-Kaderi HM, Hunt JR, Medosa-Cortés JL, Côté AP, Taylor RE, O'Keeffe M, Yaghi OM (2007) Science 316:268
13. Park KS, Ni Z, Côté AP, Choi JY, Huang R, Uribe-Romo FJ, Chae HK, O'Keeffe M, Yaghi OM (2006) Proc Natl Acad Sci USA 103:10186
14. Hayashi H, Côté AP, Furukawa H, O'Keeffe M, Yaghi OM (2007) Nature 6:501
15. Banerjee R, Phan A, Wang B, Knobler C, Furukawa H, O'Keeffe M, Yaghi OM (2008) Science 319:939
16. Kitagawa S, Kitaura R, Noro S (2004) Angew Chem Int Ed 43:2334
17. Kitagawa S, Uemura K (2005) Chem Soc Rev 34:109
18. Tanaka D, Kitagawa S (2008) Chem Mater 20:922
19. Uemura T, Kitaura R, Ohta Y, Nagaoka M, Kitagawa S (2006) Angew Chem Int Ed 44:4112
20. Férey G, Mellot-Draznieks C, Serre C, Millange F (2005) Acc Chem Res 38:217
21. Férey G (2008) Chem Soc Rev 37:191
22. Férey G, Mellot-Draznieks C, Serre C, Millange F, Dutour J, Surble S, Margiolaki I (2005) Science 309:2040
23. Seo JS, Whang D, Lee H, Jun SI, Oh J, Jeon YJ, Kim K (2000) Nature 404:982
24. Vaidhyanathan R, Bradshaw D, Rebilly JN, Barrio JP, Gould JA, Berry NG, Rosseinsky MJ (2006) Angew Chem Int Ed 118:1
25. Eddaoudi M, Kim J, Rosi N, Vodak D, Wachter J, O'Keeffe M, Yaghi OM (2002) Science 295:469

26. Serre C, Millange F, Thouvenot C, Noguès M, Marsolier G, Louër D, Férey G (2002) J Am Chem Soc 124:13519
27. Rowsell JL, Millward CAR, Park KS, Yaghi OM (2004) J Am Chem Soc 126:5666
28. Millward AR, Yaghi OM (2005) J Am Chem Soc 127:17998
29. Matsuda R, Kitaura R, Kitagawa S, Kubota Y, Belosludov RV, Kobayashi TC, Sakamoto H, Chiba T, Takata M, Kawazoe Y, Mita Y (2005) Nature 436:238
30. Rowsell JLC, Yaghi OM (2005) Angew Chem Int Ed 44:4670
31. Surblé S, Millange F, Serre C, Düren T, Latroche M, Bourrelly S, Llewellyn PL, Férey G (2006) J Am Chem Soc 128:14889
32. Maji TK, Matsuda R, Kitagawa S (2007) Nat Mater 6:142
33. Alaerts L, Kirschhock CEA, Maes M, van der Veen MA, Finsy V, Depla A, Martens JA, Baron GV, Jacobs PA, Denayer JFM, De Vos DE (2007) Angew Chem Int Ed 119:1
34. Hermes S, Schröder F, Chelmowski R, Wöll C, Fischer RA (2005) J Am Chem Soc 127:13744
35. Hermes S, Zacher D, Baunemann A, Wöll C, Fischer RA (2007) Chem Mater 19:2168
36. Shekhah O, Wang H, Kowarik S, Schreiber F, Paulus M, Tolan M, Sternemann C, Evers F, Zacher D, Fischer RA, Wöll C (2007) J Am Chem Soc 129:15118
37. Biemmi E, Scherb C, Bein T (2007) J Am Chem Soc 129:8054
38. Zacher D, Baunemann A, Hermes S, Fischer RA (2007) J Mater Chem 17:2785
39. Wu CD, Hu A, Zhang L, Lin W (2005) J Am Chem Soc 127:8940
40. Cho SH, Ma B, Nguyen ST, Hupp JT, Albrecht-Schmitt TE (2006) Chem Commun 24:2563
41. Bauer CA, Timofeeva TV, Settersten TB, Patterson BD, Liu VH, Simmons BA, Allendorf MD (2007) J Am Chem Soc 129:7136
42. Chen B, Yang Y, Zapata F, Lin G, Qian G, Lobkovsky EB (2007) Adv Mater 19:1693
43. Llabres i Xamena FX, Corma A, Garcia H (2007) J Phys Chem C 111:80
44. Alvaro M, Carbonell E, Ferrer B, Llabres i Xamena FX, Garcia H (2007) Chem Eur J 13:5106
45. Hulteen JC, Martin CR (1997) J Mater Chem 7:1075
46. Joo SH, Choi SJ, Oh I, Kwak J, Liu Z, Terasaki O, Ryoo R (2001) Nature 412:169
47. Gray DH, Hu S, Juang E, Gin DL (1997) Adv Mater 9:731
48. Fang QR, Zhu GS, Jin Z, Ji YY, Ye JW, Xue M, Yang H, Wang Y, Qiu SL (2007) Angew Chem Int Ed 46:6638
49. Horcajada P, Serre C, Vallet-Regí M, Sebban M, Taulelle F, Férey G (2006) Angew Chem Int Ed 118:6120
50. Horcajada P, Serre C, Maurin G, Ramsahye NA, Balas F, Vallet-Regí M, Sebban M, Taulelle F, Férey G (2008) J Am Chem Soc 130:6774
51. Sabo M, Henschel A, Fröde H, Klemm E, Kaskel S (2007) J Mater Chem 17:3827
52. Schmid G (1992) Chem Rev 92:1709
53. Bradley JS (1994) The Chemistry of Transition Metal Colloids. In: Schmid G (ed) Clusters and Colloids: from Theory to Applications. VCH, Weinheim, pp 459–544
54. Hitchman ML, Jensen KF (1993) Chemical Vapor Deposition. Academic Press, Principles and Applications. London
55. Sherman A (1987) Chemical vapor deposition for microelectronics. Principles, technology and applications. Noyes Publications, Park Ridge
56. Kaye SS, Dailly A, Yaghi OM, Long JR (2007) J Am Chem Soc 129:14176
57. Huang L, Wang H, Chen J, Wang Z, Sun J, Zhao D, Yan Y (2003) Microporous Mesoporous Mater 58:105
58. Greathouse JA, Allendorf MD (2006) J Am Chem Soc 128:10678
59. Hermes S, Schröter MK, Schmid R, Khodeir L, Muhler M, Tissler A, Fischer RW (2005) Angew Chem Int Ed 44:6237
60. Kim H, Chun H, Kim GH, Leeb HS, Kim K (2005) Chem Commun:2759
61. Hermes S, Schröder F, Amirjalayer S, Schmid R, Fischer RA (2006) J Mater Chem 16:2464
62. Proch S, Hermannsdörfer J, Kempe R, Kern C, Jess A, Seyfahrt L, Senker J (2008) Chem Eur J 14:8204

63. Müller M, Lebedev OI, Fischer RA (2008) J Mater Chem 18:5274
64. Schröder F, Esken D, Cokoja M, van den Berg MWE, Lebedev OI, Van Tendeloo G, Walaszek B, Buntkowsky G, Limbach HH, Chaudret B, Fischer RA (2008) J Am Chem Soc 130:6119
65. Sauer J, Marlow F, Spliethoff B, Schüth F (2002) Chem Mater 14:217
66. Hafizovic J, Bjorgen M, Olsbye U, Dietzel PDC, Bordiga S, Prestipino C, Lamberti C, Lillerud KP (2007) J Am Chem Soc 129:3612
67. Park YK, Choi SB, Kim H, Kim K, Won BH, Choi K, Choi JS, Ahn WS, Won N, Kim S, Jung DH, Choi SH, Kim GH, Cha SS, Jhon YH, Yang JK, Kim J (2007) Angew Chem Int Ed 46:8230
68. Caulder DL, Brückner C, Powers RE, König S, Parac TN, Leary JA, Raymond KN (2001) J Am Chem Soc 123:8923
69. Leary JA, Pluth MD, Raymond KN (2006) Chem Soc Rev 36:161
70. Fiedler D, Bergman RG, Raymond KN (2006) Angew Chem Int Ed 45:745
71. Pluth MD, Bergman RG, Raymond KN (2007) Angew Chem Int Ed 46:8587
72. Kawano M, Kobayashi Y, Ozeki T, Fujita M (2006) J Am Chem Soc 128:6558
73. Kaye SS, Long JR (2008) J Am Chem Soc 130:806
74. Turner S, Lebedev OI, Schröder F, Esken D, Fischer RA, Van Tendeloo G (2008) Chem Mater 20:5622
75. Kampers FWH, Engelein CWR, van Hoff JHC, Koningsberger DC (1990) J Phys Chem 94:8574
76. Opelt S, Türk S, Dietzsch E, Henschel A, Kaskel S, Klemm E (2008) Catal Commun 9:1286
77. Pan C, Pelzer K, Philippot K, Chaudret B, Dassenoy F, Lecante P, Casanove MJ (2001) J Am Chem Soc 123:7584
78. Pelzer K, Laleu B, Lefebvre F, Philippot K, Chaudret B, Candy JP, Basset JM (2004) Chem Mater 16:4937
79. Pelzer K, Vidoni O, Philippot K, Chaudret B, Colliere V (2003) Adv Funct Mater 13:118
80. Müller M, Hermes S, Kähler K, Muhler M, Fischer RA (2008) Chem Mater 20:4576
81. Sung CK, Hong W, Shi Q, Kou X, Yeung MH, Wang J, Stucky GD (2006) Adv Funct Mater 16:2225
82. Besson S, Gacoin T, Ricolleau Boilot JP (2003) Chem Commun 3:360
83. Plyuto Y, Berquier JM, Jacquiod C, Ricolleau C (1999) Chem Commun 17:1653
84. Hansen PL, Wagner JB, Helveg S, Rostrup-Nielsen JR, Clausen BS, Topsøe H (2002) Science 295:2053
85. Günter MM, Ressler T, Bems B, Büscher C, Genger T, Hinrichsen O, Muhler M, Schlögl R (2001) Catal Lett 71:37
86. Fujitani T, Nakamura J (2000) Appl Catal A 191:111
87. Kurtz M, Bauer N, Buscher C, Wilmer H, Hinrichsen O, Becker R, Rabe S, Merz K, Driess M, Fischer RA, Muhler M (2004) Catal Lett 92:49
88. Müller M, Zhang X, Wang Y, Fischer RA (2009) Chem Commun . doi:10.1039/b814241f
89. RiMoon H, Kim JH, Suh MP (2005) Angew Chem Int Ed 44:1261
90. Suh MP, Moon HR, Lee EY, Jang SJ (2006) J Am Chem Soc 128:4710
91. Cheon YE, Suh MP (2008) Chem Eur J 14:3961
92. Hwang YK, Hong DY, Chang JS, Jhung SH, Seo YK, Kim J, Vimont A, Daturi M, Serre C, Férey G (2008) Angew Chem Int Ed 47:4144
93. Henschel A, Gedrich K, Kraehnert R, Kaskel S (2008) Chem Commun:4192
94. Becker R, Parala H, Hipler F, Tkachenko OP, Klementiev KV, Grünert W, Wilmer H, Hinrichsen O, Muhler M, Birkner A, Wöll C, Schäfer S, Fischer RA (2004) Angew Chem Int Ed 43:2839